Laser Induced Graphene on Lignin Upgraded Stretchable Polymer Films

by

Kaustubh Sinha

A thesis submitted in partial fulfilment of the requirements for the degree of

Master of Science

in

Photonics and Plasmas

Department of Electrical and Computer Engineering

University of Alberta

Abstract

Graphene is a unique material which exhibits exceptional electrical, mechanical and chemical properties owing to its two-dimensional structure. A global effort has been made to produce this material in the past decade, and researchers have come up with several fabrication techniques. Although, laser induced graphene (LIG) is a relatively novel fabrication technique to produce graphene, LIG has been demonstrated for various applications on a variety of substrates such as wood, polyimide films and DVD disks which are either non-renewable and flexible or environment friendly but mechanically rigid. This thesis describes the fabrication of a lignin enhanced stretchable polymer matrix which is used to produce LIG via a commercially available scribing laser. It was found that marginal addition of lignin to create the polymer matrix yields better LIG with increasing lignin concentration. Also, slower laser trace speeds yield higher quality porous LIG structures with fewer structural defects and highly multilayer LIG. To demonstrate the application for flexible electronics, the LIG was deployed as a pressure sensor as a proof of concept.

Preface

This thesis is an original work by Kaustubh Sinha under the supervision of Dr. Xihua Wang at the Department of Electrical and Computer Engineering, University of Alberta.

The thesis is based on a work that is yet to be published in a journal.

For the work described in this thesis, I was responsible for the experimental design, device fabrication, data analysis and drafting the manuscript. Dr. L. Meng assisted with tools to be used for device fabrication and characterization. Dr. X Wang supervised and will serve as the corresponding author on the publication.

Acknowledgements

Science has been a subject very close at heart to me. There are those who excel at others subjects in academia and put science aside as a very analytical and categorical form of study. Those on Earth who really devote themselves towards a deep dive into this marvelous study of nature come to value the understanding that comes with, and appreciate the beauty of the truth when it reveals itself in the most interesting and intuitive forms.

While I strived to do research as a Masters' student; research that was as great as my ambitions are, the work I accomplished falls short to be described as a great contribution. In my journey through the Masters' education which started about two years ago, I never knew about the several mistakes I would commit. These opportunities have made me a better student and a better researcher leaving me with improved tools to intellectually engage in better scientific study.

I thank my supervisor, Dr. Xihua Wang, for providing me an open field to develop my research attributes. I admire his coherent thinking and my gratitude goes to him for always being available for guidance. Sincere thanks go towards my committee members, Dr. Manisha Gupta, Dr. Karthik Shankar and Dr. Xingyu Li.

A heartfelt Thank you to my father and mother. Their endless love and support towards me and my educational freedom form the tenets of my ambition in creating something better for this world. Thanks to my little brother, Amogh, for his love, respect and admiration towards my career choices which always drove me towards outperforming myself.

Thanks to my colleagues Dr. Lingju Meng, Mr. Qiwei Xu and Mr. Carson R. Dick for their valuable insights and guidance. Sincere thanks to Mr. Farsad Imtiaz Chowdhury for his assistance and experienced guidance.

I offer much gratitude to my dearest friends Mr. Arturo Mora Gomez, Mr. Shubhendra Trivedi, Mr. Nima Mehdizadeh, Ms. Srujita Karodi, Mr. Shubhankar Choudhary, Mr. Arjun Anil, Ms. Malika Agarwal, Ms. Johanna Sari, Ms. Kritika Aima, Mr. Wasel Ur Rahman, Mr. Aadil Khan, Ms. Priyanka Maripuri, Mr. Qiwei Xu, Mr. Steve Okocha, Mr. Shuce Zhang and Ms. Sarashmi Sarker, for being there for me in times of hardship and otherwise with their love and support.

I also sincerely thank and offer gratitude to the University of Alberta for providing me this opportunity and assistance in times of need, to help me fulfil my funding requirements. The city of Edmonton will always be close to my heart as it is where I started my life with my independent earnings. A city new to me, where I experienced my first snowy winter, its people have offered me much warmth.

Table of Contents

List of Figures

Chapter 1

Introduction

1.1 Introduction to graphene

Allotropy is a property of chemical elements to assemble in different physical forms/ structures. Carbon, the most fundamental element to complex life on Earth, has a commensurate number of allotropes such as diamond, graphite, graphene, amorphous carbon, carbon nanotubes, lonsdaleite, fullerenes etc. Each of these allotropes have exceptional mechanical and chemical properties but graphene is the most interesting allotrope of carbon as it is a purely two dimensional (2D) hexagonal matrix with carbon molecules at every vertex akin to a honeycomb structure. The dimensionality of graphene gives it extremely advantageous electronic, optical, mechanical and thermal properties. Upon its first isolation by the Andrew Geim group in 2004 [1], this ground-breaking demonstration was awarded the Nobel Prize in Physics in 2010. Advertised as a "wonder material", graphene was purported to find applicability spanning a wide spectrum of industries including computing, energy and medicine. The exfoliation technique by Geim's group was performed on graphite, which is another allotrope of carbon discovered in 1564, that comprises of stacked layers of graphene bound together via van der Waal (vdW) forces of attraction. This discovery initiated the graphene industry. Ideal graphene cannot always be obtained in perfectly continuous single sheets, there can be multiple layers, defects and edge sites where the structure gives rise to other characteristic properties.

1.1.1 Chemical Properties

A carbon atom has 6 electrons, hence its electronic configuration is given by $1s^2 2s^2 2p^2$, where 4 electrons in the 2nd shell are available for bonding. But in the graphene structure, each carbon atom is surrounded by 3 other carbon atoms, hence, after forming 3 covalent bonds, there is an extra π(pi) electron left. Fig. 1.1a shows the characteristic σ(sigma) bond length of 0.14 nm in an atomic resolution image of graphene, while the Fig. 1.1b shows a single layer of graphene supported between two gold electrodes. These 3 covalent bonds lead to sp^2 hybridization of the carbon atoms where the s, p_x and p_y orbitals contribute towards a planar symmetry giving the characteristically observed 120° bond angle formed between the hybrid σ(sigma) bonds. There is an additional p_z orbital perpendicular to the graphene plane due to the extra electron above and below the graphene sheet, that forms π(pi) bonds. These pi bonds hybridize together to give band structure which gives exotic electronic properties to graphene [2,3].

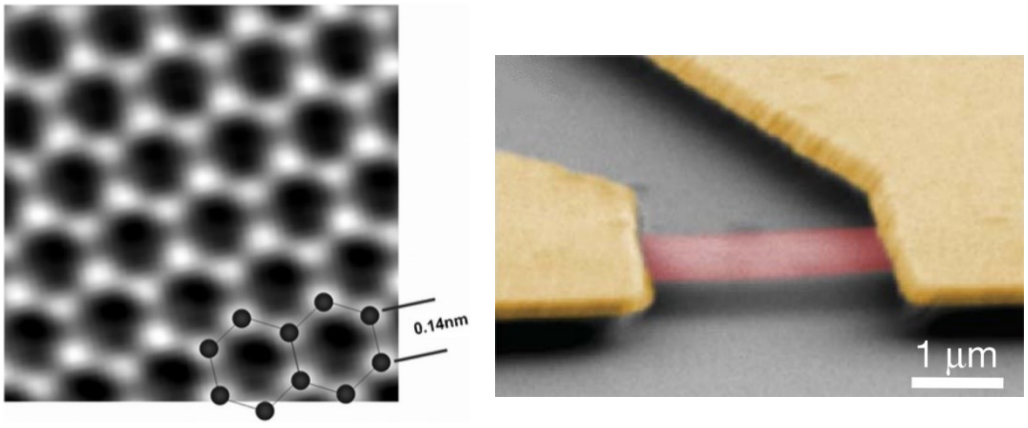

Figure 1.1: (a) Atomic resolution image of structurally perfect Graphene. The carbon atoms appear as white in the honeycomb lattice. **Reprinted from [4] with permission from Royal society of Chemistry.** (b) False-colour SEM image of single layer graphene (red) suspended 150 nm above SiO_2/Si substrate (grey) and supported by two gold electrodes (yellow). **Reprinted from [5] with permission from Nature.**

1.1.2 Electronic Properties

Graphene has an electron mobility that goes up to 200,000 $cm^{-1} \cdot V^{-1} \cdot s^{-1}$ at room temperature with a carrier density of 1012 cm^{-2}, where electron and hole mobilities are similar. Mobility is independent of temperature in the range of 10 - 100 K [6,7] implying defect scattering is the dominant scattering mechanism. These electrons can cover micrometre distances without scattering even at room temperature, [8] hence this unhindered flow of electrons leads to such interesting electrical properties. The corresponding resistivity of the graphene sheets is 10^{-6} Ω·cm [9], which is the lowest of any material at room temperature.

1.1.3 Mechanical Properties

Thermal conductivity of Graphene has been calculated to be in the range 1,500 – 2,500 $W \cdot m^{-1} \cdot K^{-1}$ [10] which is significantly higher than most materials and another allotrope of carbon, diamond which has a thermal conductivity of 2,200 $W \cdot m^{-1} \cdot K^{-1}$ [11]. As seen in Fig. 1.1a, graphene also possesses unconventional mechanical properties, with a bond length of 0.14 nm [12], it is the strongest material that has ever been tested that exhibits a tensile strength of 130 GPa and a Young's modulus of 1 TPa (150 million psi) [13]. Fig. 1.1b shows a single layer of graphene supported by Au electrodes suspended on a SiO_2 substrate, this proves a single atom thick layer of graphene has the molecular strength to exist in such a physical form. But most of these exceptional properties such as high strength occur only in near perfect manufactured/ isolated sheets of graphene. Defects in the graphene structure can make it brittle (fracture toughness of 4 MPa·√m).

1.1.4 Other properties

Other types of graphene can be organized by division into number of layers and defect sites. First, considering the number of layers, properties described in the section above are exhibited by the single layer graphene (SLG) formed by a 2D layer of carbon atoms, which is ideal state of graphene. Multilayer graphene (MLG) implies >2 layers of graphene stacked on top of each other. MLG exhibits various exotic electronic properties compared to SLG which does not have a band gap. Bilayer graphene- two layers of graphene has a zero bandgap but the bandgap can be made widely tuneable [14].

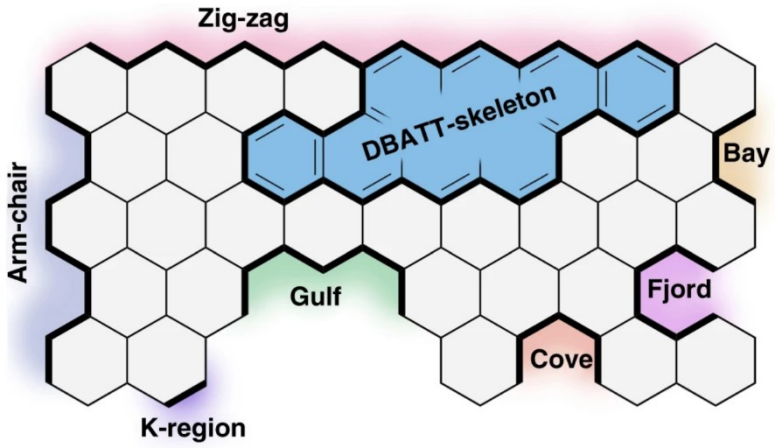

Figure 1.2: Edge structures in Graphene. **Reprinted from [15] under the Creative Commons - BY License.**

Imperfect graphene with defects in its structure also exhibits special chemical properties in these defect regions[16], where the chemical reactivity of the whole structure can be modulated via the type and number of functional groups that are attached to these defect sites. The edges of the graphene sheets have several topologies as seen in Fig. 1.2, each of which exhibit special chemical reactivities not discussed here.

The versatile and exotic properties of graphene bestow it diverse functionalities for use in a plethora of applications. Graphene can find utility in thermal management, anti-corrosive

coatings, bionic materials, electro-magnetic shielding material for military applications, drug delivery systems, biological sensors and bionic materials due to its biocompatibility [17], light emitting diodes, solar cells, Infrared (IR) transparent materials, supercapacitors, batteries, superconductors, magnetic sensors and metal matrix composites. Graphene can be used for antireflection coatings in solar cells/ panel displays/ phones/ laptops, organic electronics and lighting, transparent conductive films and study of RNA and DNA sequences. These applications indicate a huge potential industrial demand for graphene with its industry valued at USD 42.8 million in 2017 which is expected to grow at a rate of 38% by 2025 [18].

1.2 Overview of graphene production methods

Graphene is a 2D molecule, which is present in nature in the form of graphite which has multiple sheets of graphene stacked on top of each other that are held together by vdW forces of attraction. Owing to its structure the graphene molecule is not found in nature in its natural state -because larger 2D sheets of such a material cannot naturally come into existence. As soon as the 2D crystals cross a certain size, the phonon density increases and vibrations result in the collapse of the 2D material into 3 dimensions hence making it impossible for larger sheets of the 2D material to occur naturally.

There are several methods to manufacture graphene, which involve physical and/ or chemical processes. The fabrication methods can be divided into two broad categories: top-to-bottom (TTB) and bottom-up (BU) approaches. Overtime, research on this material has led to several unique techniques and processes in both approaches which are used to extract or fabricate graphene. As seen in Fig. 1.3, the TTB approach utilizes the graphitic structure to produce graphene using several chemical and mechanical methods whereas the BU approach

employs chemical methods to build/ fabricate graphene from carbon molecules onto certain substrate materials.

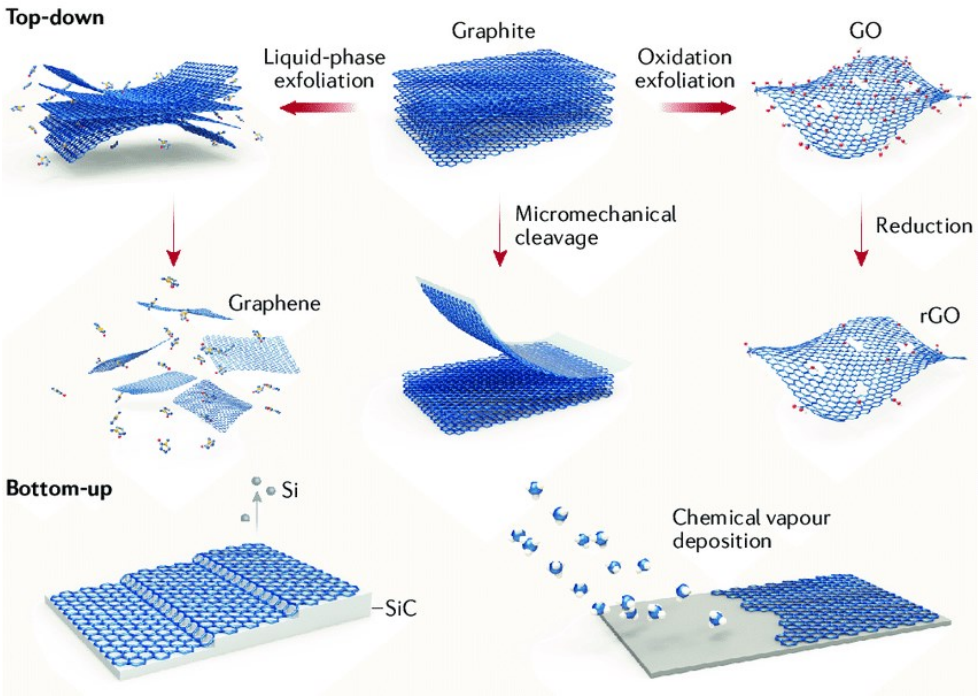

Figure 1.3: Schematic illustrating the different pathways to fabricate graphene. **Reprinted from** [19] **with permission from Nature reviews Chemistry.**

1.2.1.Exfoliation

Exfoliation is a TTB approach. This technique deals with isolating layers of graphene via either repetitive removal of several layers or one-time removal of a few layers or even a single layer. First demonstrated in 2004 by Andre Geim [1], an adhesive tape was used to exfoliate a single layer of graphene from a sample of highly oriented pyrolytic graphite. After multiple exfoliating steps, "few-layer graphene" could be obtained up to a size of 10 μm, however larger, visible sheets (100 μm) of graphene (thickness >= 3 nm) could be isolated on top of a silicon wafer. The vdW attractive force of 5.9 kJ/ mol between the different layers of graphite, facilitated by the pi-bonds, can be easily overcome by the adhesive force of the tape hence isolating the layers of graphene. Contrarily this tape exfoliation method, being one of the first methods to extract a few layers of graphene is also the most inexpensive technique. Other techniques to exfoliate graphene may include using a single crystal diamond edge saw that can cleave layers of graphene [20] or rapid heating of graphene oxide followed by exfoliation resulting in carbon powder, where small size layers of graphene can be isolated, electrochemical exfoliation [21].

Several researchers have also explored using graphene oxide (GO) as a precursor to produce graphene. Graphite is oxidized to GO using Hummers' method which is followed by exfoliation to give single layer graphene oxide that can be up to 1 μm in length. This single layer of GO can be thermally annealed or treated with Hydrazine to give a graphene referred to as reduced GO (rGO) [19,22,23]. Fig. 1.4a depicts the molecular structures of graphene , GO and rGO where Fig. 1.4b exhibits the removal of hydrogenated hydrocarbons via thermal annealing/ reduction of GO. rGO has a great number of structural defects and has poor quality which compromises its electrical properties with carrier mobility extremely small relative to SLG at 1 $cm^2 \cdot V^{-1} \cdot s^{-1}$ [24]. The quality of rGO has now been improved substantially by

applying temperatures below 10°C before the oxidation and quenching step in the Hummers' method leading to a reduction in the number of carbons that escape as CO_2 improving structural defect density upon oxidation giving higher carrier mobilities up to 1000 $cm^2 \cdot V^{-1} \cdot s^{-1}$ [25].

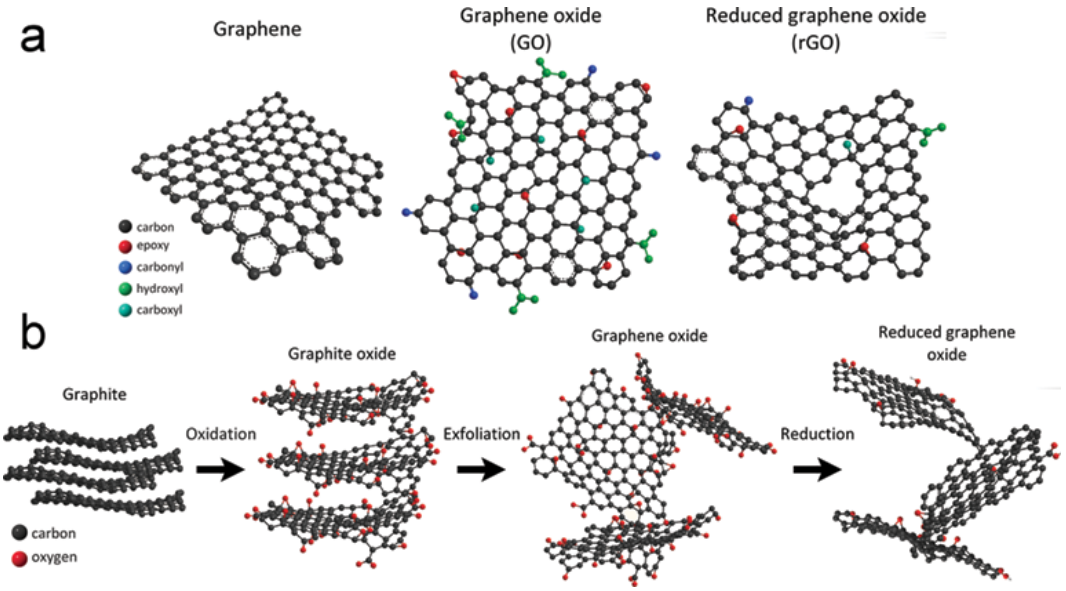

Figure 1.4: Molecular structures of (a) Graphene (b) Graphene oxide (with several oxygenated hydrocarbons) and (c) reduced Graphene Oxide (rGO). **Reproduced from** [26] **under the Creative Common – BY license.**

The liquid phase exfoliation process can principally avoid significant disruption of the graphene plane. The principle of the process is to break the vdW forces between the graphene layers using external forces, hence, the liquid exfoliation process is often accompanied with ball milling, sonication or shear mixing [27,28,29]. Ball-milling is different from the other processes as it takes place in a suspension or by using a solid material after which dispersion is used to separate out graphene flakes. Sonication and shear mixing are performed directly in solution. Graphene flakes produced via the liquid phase exfoliation have better electrical properties compared to native rGO by two orders of magnitude at 100 $cm^2 \cdot V^{-1} \cdot s^{-1}$. However, this is a low yield process which results in a mix containing a higher proportion of MLG

compared to SLG. Moreover, these processes also cause partial oxidation and/ or fragmentation hence causing inevitable damage to the graphene structure.

Electrochemical exfoliation has now emerged as the most promising and cost-effective liquid exfoliation technique for large scale production of high-quality sheets of graphene [30]. The process involves using graphite rods as electrodes in a solution of specific chemical electrolytes, the molecules of which intercalate between the graphitic layers upon the application of an electric potential. After which gaseous expansion results in exfoliated graphene sheets that can be collected using vacuum filtration and dispersed in DMF and NMP where the graphene sheets are stable for several weeks. These large sheets (5-10 μm) have a high yield of ~75% with few defects and carrier mobilities around ~405 $cm^2 \cdot V^{-1} \cdot s^{-1}$. Moreover, by using an AC voltage, production rates can be further improved as the exfoliation would take place at both electrodes.

There is still a need to produce higher quality graphene with higher yield by reducing structural defects and O:C ratio. New techniques for improving the exfoliation process to overcome the stated problems, such as using microwave radiation [31], show promise for exfoliation techniques to obtain high quality graphene in the future.

1.2.2 Epitaxy

Epitaxy is a BU approach. Epitaxial growth is a deposition process where a desired material is built layer by layer using chemical methods of deposition. With effective chemical reactions, highly pure crystals with very few defects can be manufactured using this process. The processing of chemicals in this process proceeds in a timely manner where reactive gases

are introduced into the reaction chamber with vacuumed intervals for separation in layer forming reactions.

Epitaxial growth of graphene can be used to couple a single 2D sheet of graphene in place onto chemically modified surfaces using vdW forces of attraction [32,33]. One process involves growing graphene on silicon carbide (SiC) wafers followed with graphitization by annealing at temperatures > 1000°C under ultrahigh vacuum. These crystalline sheets can reach sizes up to several hundred micrometres. The charge carrier mobility depends upon the substrate on which these sheets are grown, which is the reason for the large difference in the room temperature mobilities of 500 - 2,000 $cm^2 \cdot V^{-1} \cdot s^{-1}$ 1 on Si terminated surfaces to 10,000-30,000 $cm^2 \cdot V^{-1} \cdot s^{-1}$ on C terminated surfaces. [34] The high cost of SiC wafers prevents their use for mass production of graphene, hence making it suitable for laboratory study applications.

1.2.3 Chemical Vapor Deposition

Chemical vapor deposition (CVD) is the most promising technique employed to produce large sheets of graphene. It is a BU technique in which 2D graphene films are formed via thermal decomposition of carbonaceous sources after which the carbon atoms assemble into honeycomb structures, mostly on transition metals such as Ni or Cu. Cu is often preferred as the main substrate since it has a gentle catalytic activity and due to the low solubility of carbon atoms into copper substrates [35]. After etching Cu using etchants such as $FeCl_3$, polymer supports such as polymethylmethacrylate (PMMA) are used to transfer the graphene onto SiO_2 substrates. The PMMA is then dissolved using acetone to finish the transfer process. Another study involving CVD of graphene onto a Cu substrate using thermal decomposition of CH_4, reported a carrier mobility of 4050 $cm^2 \cdot V^{-1} \cdot s^{-1}$ [36]. This process employed selective

heating of the Cu substrate by electric voltages to produce large sheets of graphene from 23 cm to 100 cm [37. This processing technique has been used to integrate graphene onto the ubiquitous CMOS technology to obtain large monolayer sheets of graphene with negligible defects [38]. Different types of CVD processes have also claimed to produce monolayer graphene in a quick and cost- effective manner [39]. CVD techniques produce graphene that is mostly polycrystalline over the whole area that is composed of single-crystalline domains with varying lattice orientation. This occurs due to the merging of several independently grown graphene sheets that are left with grain boundaries at the junctions forming 5 or 7 carbon rings, which also greatly affects the material and electronic characteristics of graphene. Carrier mobilities of 40,000 - 65,000 $cm^2 \cdot V^{-1} \cdot s^{-1}$ were achieved by a study, where addition of surface oxygen to the Cu substrate suppressed the nucleation density forming up to 1 cm long sheets of graphene within 12 hours [40].

1.3 Laser-induced graphene (LIG)

Recently, graphene has been achieved by using lasers. This process employs a laser that uses photons which strike specific carbonaceous substrates and degrade their surface into aromatic structures that come together to resemble the graphene structure. The presence of carbons in the sp^2 hybridized aromatic structures of graphene, necessitates the selection of specific substrates for LIG that have these structures embedded in their molecular structure prior to the lasing process for the formation of graphene to occur. Hence carbonaceous substrates such as polyimide (PI), polyetherimide (PEI), DVDs, wood, paper all of which have aromatic molecular structures that contribute to graphene are used to produce the graphene structures which can take fragmented, flaked, fibrous or tubular forms. A variety of laser sources can also be used to degrade these carbonaceous substrates into LIG. Lasers with

wavelengths ranging from UV [41]to far IR [42] have been employed for laser induction of graphene from the previously mentioned substrates.

1.3.1 The production of laser-induced graphene

Laser sources use photons to degrade material substrates to graphitic structures. From UV lasers operating at a wavelength of 305 nm to CO_2 IR lasers at 10.6 μm[42,43], all have been employed to produce intermediary amorphous carbon [43] or graphene. The lasers used in these processes employed parameters like different power and spot size diameters [42,43]. Different types of lasers such as scientific lasers, laser cutters and DVD disk lasers have also been employed to produce LIG.

While most of these works [44,45,42] discussed single scribing of the laser to obtaining LIG, another work found that using multiple lases onto a substrate while also varying the focus ("Defocus method"), diverse materials such as cross-linked polystyrene, epoxy, and phenolic resin could be used to produce LIG. This work described a two-stage process where the first iteration of lasing was used to convert these substrates into amorphous graphene as an intermediary stage after which further multiple lasing resulted in the formation of graphene structures. Due to the laser focus having the shape of a hyperbolic cone, different levels of focus could be achieved just by changing the distance between the laser and the substrate employed for LIG production. This is shown in Fig. 1.5, where employing the defocus method means the focus region of the trace can be increased or decreased by adjusting the height/ distance from the focal plane.

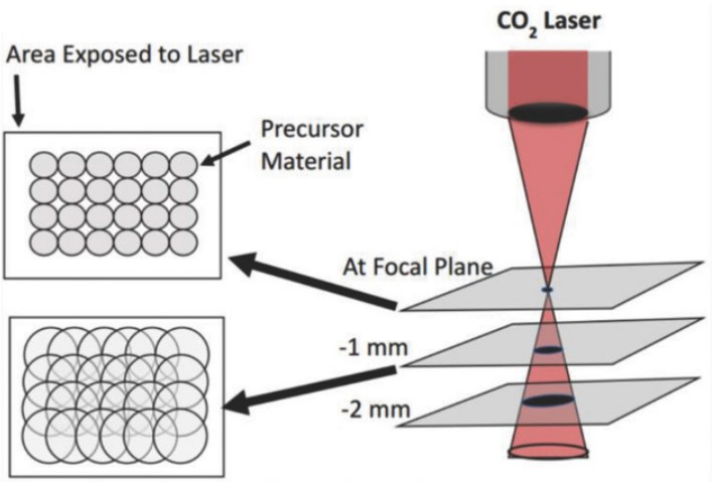

Figure 1.5: The schematic illustrates the defocus method that is utilized in the multiple lasing process. As seen, different levels of defocus, such as the 1mm defocus result in the enlargement and overlap of the are traced by the laser. **Reprinted from** [43] **with permission from ACS Nano.**

Early studies employed the use of substrates such as PEI to form LIG [10.1038/ncomms6714] and other similar substrates such as sulfonated poly(ether ether ketone), polysulfone, and polyethersulfone [46,47]. Over time a range of substrates ranging from synthetic Phenolic resins and their composites [48] to naturally occurring resins found in wood [49] have been used to obtain LIG. Fig. 1.6 shows a recent work which developed a method capable of converting most carbonaceous materials into LIG using a CO_2 IR laser under ambient atmospheric conditions[43]. Different substrates like wood, bread, potatoes and papers were shown to produce LIG implying the variety of applicative surfaces for LIG.

The research done on converting wood to LIG employed an inert atmosphere and suggested that higher lignin content in wood is more favourable towards producing better quality LIG as compared to cellulose/ hemi-cellulose. Materials that easily decompose into volatile compounds, due to a high cellulose content can be used for LIG process upon pre-treatment using fire retardant or charring to convert them to the intermediary amorphous carbon stage prior to lasing. This opens up the process to a diversity of materials such as bread, muslin

cloth, wood, cotton paper and cardboard that can be used for LIG production under ambient atmosphere with improved conductive properties and sheet resistance as low as ~5 $\Omega \cdot sq^{-1}$.

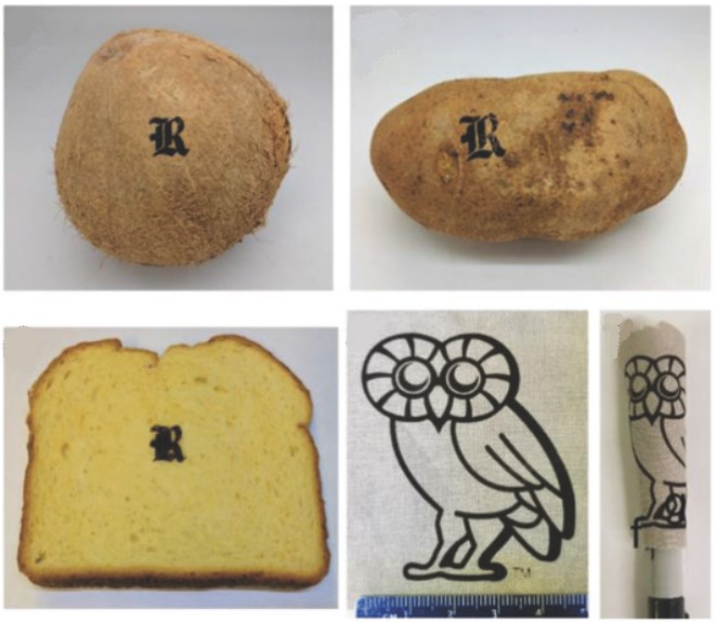

Figure 1.6: Different substrates that have been employed to produce LIG which enables a variety of applications. **Reprinted from** [43] **with permission from ACS Nano.**

Laser patterning of graphene is advantageous in two major ways: it enables laser patterning LIG onto a variety of substrates allowing for flexibility in the use of materials that are being employed for the purpose of producing LIG. Second, it can also be deployed onto roll to roll processes which enables large scale, mass manufacturing of LIG sheets that may find use in several applicative technologies such as sensors which have already been researched in various studies.

1.3.2 The properties of laser-induced graphene

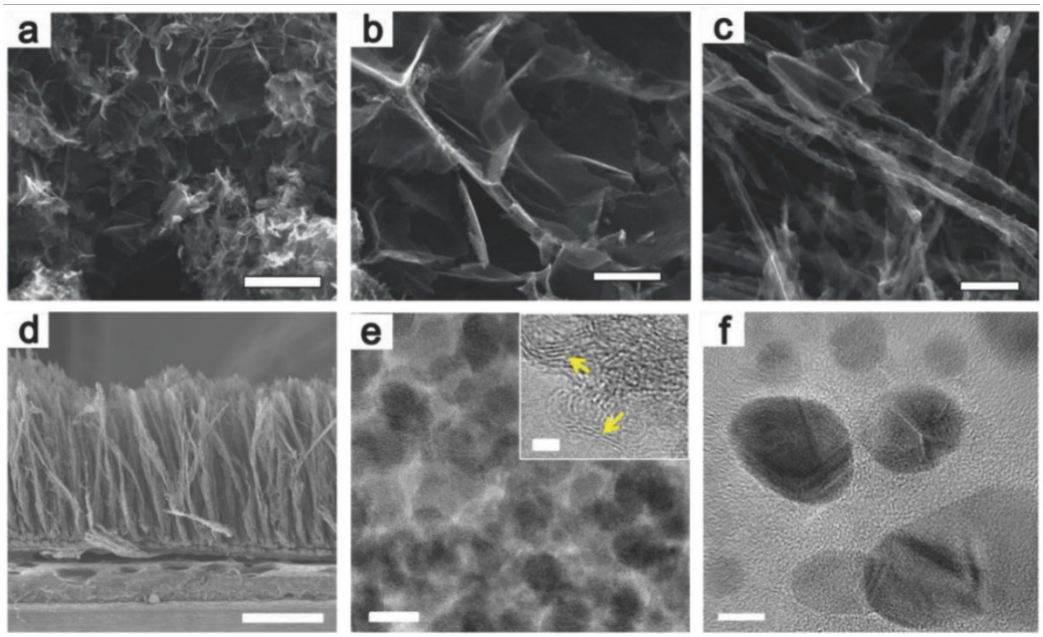

Figure 1.7: SEM images of the different LIG structures. a) Inhomogeneous macroporous foams; scale bar, 5 µm, b) corrugated tiles; scale bar, 1 µm, c) tubes; scale bar, 500 nm, and d) fiber forests; scale bar 500 nm. a–c) d) e, f) Nanomaterials derived from PTFE using a 9.3 µm CO_2 laser. e) Spherical fluorinated graphene; scale bar, 50 nm in (e) and 1 nm in the inset. f) Fluorinated nanodiamonds; scale bar, 5 nm. **Reprinted from** [50] **with permission from Advanced Materials – Wiley Online Library.**

The substrate chosen to produce LIG greatly influences its properties. This is because the phenolic structures present in the precursor substrates have different functional groups attached to them which if not removed during the lasing process, exhibit different behaviour and alter the properties of LIG when they interact with other external molecules. Removal of these additional functional groups which influence the properties of LIG is very hard. Considering most of the substrates used for producing LIG are highly carbonaceous with primarily hydrocarbon or polymeric content, the resulting functional LIG mostly comprises of only oxidized species that serve as impurities to the otherwise pure LIG.

The properties of LIG are slightly different than monolayer graphene due to its fabrication process. Graphene formed using the laser induction process is not an isolated sheet of 2D material but a 3D structure that can range from a few layers to multiple layers of graphene stacked mostly in random orientations. LIG formed via laser induction can take several physical forms depending on the substrate that has been used. As seen in Fig. 1.7, LIG can take the form of foam (porous 3D MLG) and flakes [42], fibres [51], which implies these structures are independently flexible and strong at the microscale but on a macro-scale they are highly fragile and tend to break or smear off upon the application of external force or pressure that exceeds a certain limit. The flexibility [52] of the flakes allows the LIG obtained on flexible substrates such as PI allows it to be used as microsupercapacitors or electrodes in separate applications [45,53]. The characteristics of the LIG produced on most substrates are gauged via Cyclic Voltammetry (CV) tests or $\Delta R/R$ [54] resistivity tests for assessing capacitive properties or current-voltage characteristics respectively, which continually indicates good electrical properties of LIG.

The surface characteristics of materials greatly define their physical and chemical properties such as reactivity, hydrophobicity or photophysical response [55,56,57]. These surface characteristics arise from the porous structure of the LIG which has been explored in great depth in recent studies and has shown to be modulated either via different laser induction parameters such as speed and power or by manipulating the material composition and structure. In the first strategy, the gaseous evolution during the lasing process results in the formation of the porous structure, hence larger the laser power, higher the gaseous liberation resulting in a larger pore size [42]. However, after a certain threshold, increasing the laser power causes damage to the structural threshold [58]. The second strategy involves using a mix of materials, where one component ablates creating the porous structure while the second component

transforms to graphene upon lasing. A study developed an ordered mesoporous LIG structure by lasing a film prepared using self-assembly of a block copolymer (BCP) and resols [59].

1.3.3 The applications of laser-induced graphene

Prior work has shown that LIG exhibits useful properties that can find applications in energy storage microsupercapacitors (MSCs), microfluidics, electrocatalysts, wearable electronics and in several sensing applications.

Miniaturized energy storage devices are now necessary due to the growth of portable and wearable technology. Microsupercapacitors are advantageous over micro-batteries as they have faster charge/ discharge cycles, high energy density and high durability over time [60,61,62,63]. The first work on LIG was used to demonstrate a MSC on a sheet of PI. CV tests indicate the energy is stored by the formation of an electrochemical double layer, where even with a high voltage scan rate scan rate of 10,000 $m \cdot V \cdot s^{-1}$, the pseudo-rectangular shape was maintained and the specific areal capacitance (CA) was retained over 1 $mF.cm^{-2}$, indicating the applicability of the device in high power electronic applications. With a high capacitance in the range 1.3- 3.9 $mF \cdot cm^{-2}$, this LIG MSC outperformed other carbon based MSCs [64,65,66]. To further enhance the capacitance of carbon based MSCs, two methods have been suggested, a chemical and a physical method. The chemical method involves doping LIG with heteroatoms to change its electronic properties and wettability. A capacitance of 16.5 $mF \cdot cm^{-2}$ was reported [45] after doping LIG with Boron using Boric acid. A similar improvement in capacitance of ~11% was achieved using plasma treatment to increase the oxygen content which improved the surface wettability. The physical method just involves integrating the capacitors in series or parallel to maximize capacitance and improve the output voltage [67].

LIG properties such as flexibility, porosity and electrical conductivity can be exploited in microfluidic applications to be used either as channels or electrodes. There are multiple techniques that have been reported for the formation of porous channels, these involve a curing process which is followed by removal of organic residues [68,69]; direct hierarchical self-assembly of BCP [70]; and optical lithography techniques using multiphoton absorption polymerization and stimulated emission depletion [71,72]. As seen in Fig. 1.8, a trench has been created in BCP using laser induction with a polydimethylsiloxane (PDMS) seal on top, rendering as a microfluidic channel.

LIG on PI was exploited as an electrode to showcase its application as a membrane less microfluidic redox battery (MRB) as the power source for wearable electronics. The MRB has microchannels with laminar flow of anodic and cathodic fluids that interact at the LIG electrode creating a power density of 0.75 $mW \cdot cm^{-2}$ at a current density of 1.75 $mA \cdot cm^{-2}$.

Electrocatalysts for a wide range of applications have been developed by forming a composite with the high surface area LIG. A recent work on water-splitting to obtain H_2 as a renewable energy carrier has attracted great research interest [73]. High energy efficiency is the primary goal of this research, achieved by lowering the operational potential while delivering high current density. Development of higher-activity catalysts and higher-capacity materials coupled with research on other catalytic systems such as thermal or electrochemical carbon dioxide reduction reactions and alcohol oxidation processes will improve catalytic applications of LIG.

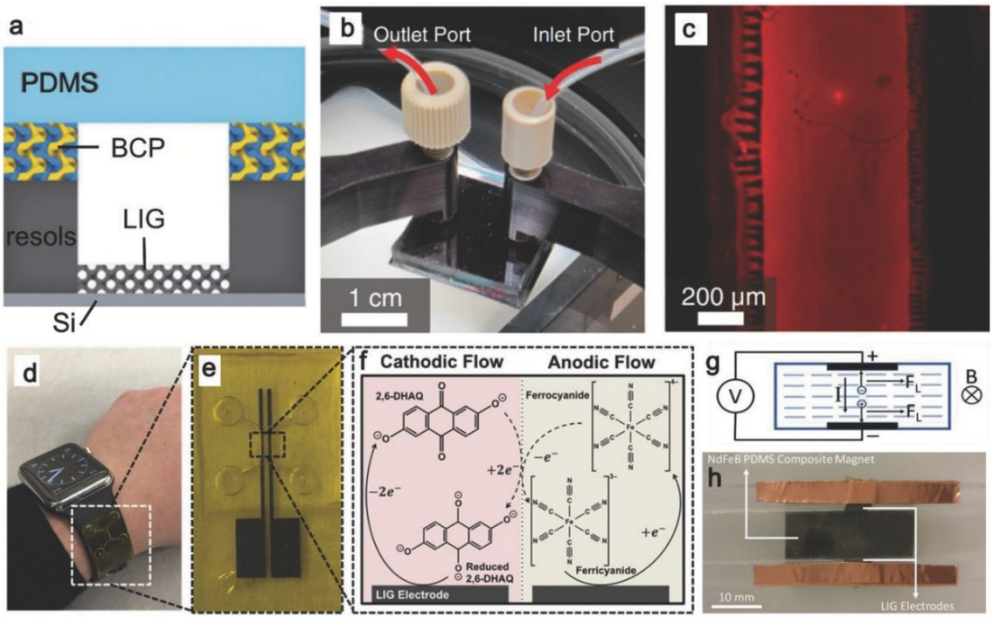

Figure 1.8: LIG in microfluidic devices. a) Schematic illustration of the microfluidic channel design. b) Optical image of a microfluidic device fabricated by laser writing, then transferred to a probe station. c) Fluorescence optical micrographs of tetramethylrhodamine (TRITC) dye dissolved in DMSO passing through the microfluidic channel. d) A photo showing the concept of the membraneless microfluidic redox battery (MRB) as a potential power source for wearable devices. e) Image of the MRB showing the channels in the microfluidic device for controlled laminar flows. f) The half-reactions in the anodic and cathodic flow, respectively, in the microfluidic channel network. g) Schematic and working principle of a typical Magnetic hydrodynamic (MHD) pump. h) A photograph of the fabricated MHD pump. **Reprinted from** [50] **with permission from Advanced Materials – Wiley Online Library.**

The work shown in Fig. 1.9, demonstrates a highly stretchable sensor fabricated by mixing LIG extracted from lasing on PI with conductive poly(3,4-ethylenedioxythiophene):polystyrene sulfonate (PEDOT:PSS) and elastic polymer polyester-polyurethane (PU) composites [74]. The extracted LIG powder is mixed with a premixed mixture of both the polymers to obtain a conductive LIG - PEDOT:PSS ink which was then micro printed onto polyurethane films. These Stretchable- Microsupercapacitors (S-MSCs) are reported to have >10-fold improvement over the previous directly laser induced MSCs attributed to higher density of the LIG content in the printed electrodes.

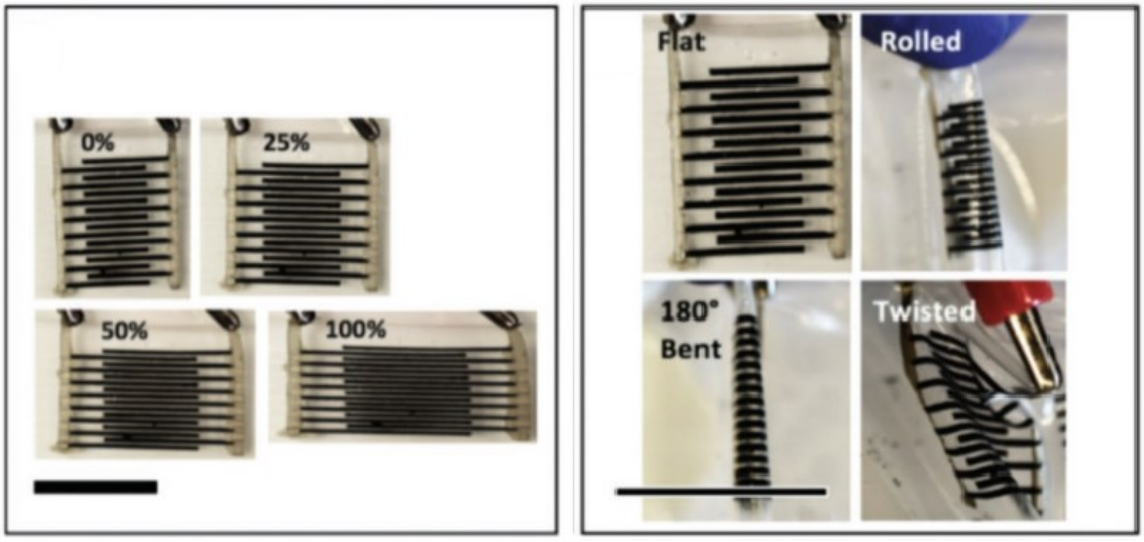

Figure 1.9: A demonstration of the flexibility of the wearable sensor. (a) As can be seen the sensor exhibits no damage to the printed pattern upon stretching at 0%, 25%, 50% and 100%. (b) Bending/twisting tests in 0% bending (flat), 180° bending, over 180° bending (rolled), and arbitrary twisting. **Reprinted from** [74] **with permission from Advanced Materials Technologies– Wiley Online Library.**

Global research efforts have led to the development of several sensors based on LIG or modified LIG materials that can sense a variety of stimuli. Fabrication of these sensors is cost-effective and exhibits great potential for mass manufacture using roll-to-roll processing over conventional lithographic approaches. LIG can be employed to sense humidity, strain, UV radiation and biological phenomena like ECG, hydration and temperature among a variety of other sensory inputs.

A recent work fabricated an LIG based non-contact moisture-responsive electronic skin matrix, where the LIG formed by laser reducing GO (LRGO) acts as the electrode and the pristine GO film acts as the sensing layer [75]. The LRGO is present in the form of a 4 × 4 sensor matrix which can detect direct human breath, finger touches and humidity via a change in impedance. The change in relative humidity (RH) from 15% to 95% is interpolated into an impedance change of up to four orders of magnitude, making it highly sensitive. This change

in impedance was due to the adsorption of water molecules onto the GO film which increased conductivity upon ionization forming hydronium ions (H_3O^+).

Strain sensors are sensors that detect lateral strain on a material in 1 dimension. Achieving high gauge factors is an issue with strain sensors. Recently, a strain sensor with that had self-locked overlapping LRGO sheets with a high gauge factor (>400) was fabricated by laser induction[76]. The LIG strain sensors work by producing a resistive response that is proportional to the strain applied. This sensor was locked in place with a thin film of PDMS on top of the fragile LRGO to prevent any damage due to strain. Strain sensors with ultra-high gauge factors of up to 673 have also been developed [77] based on the crack directions and electrical characteristics. The epidermal electronic skin (ultrahigh gauge factor of 673) was created by laser induction on a GO film substrate which could be transferred onto any substrate upon chemical treatment [77].

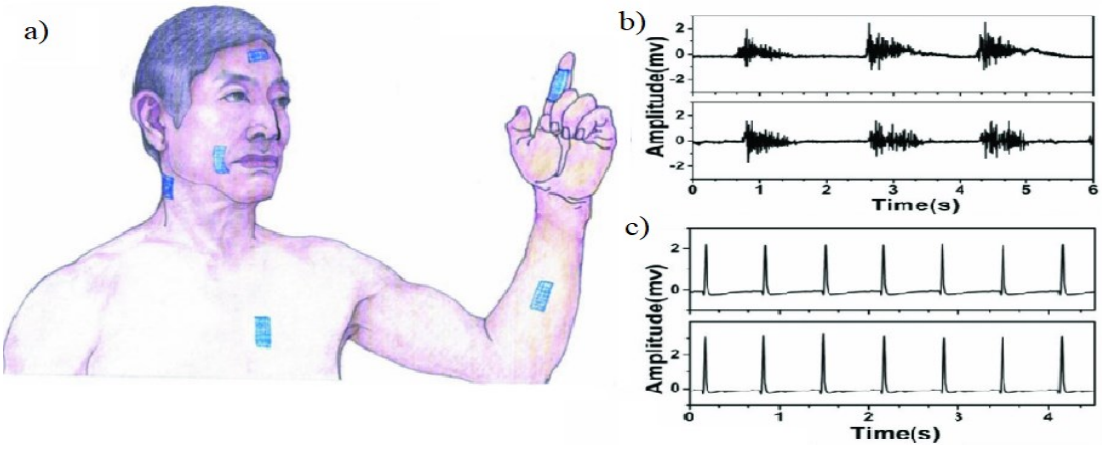

Figure 1.10: (a) Schematic illustration shows the various locations the devices are mounted like the forehead, chest, forearm, face, neck and finger to monitor the various electrophysiological activities. (b) EMG signals measured at the forearm using the LIG sensors (top) and conventional gel electrodes (bottom) (c) ECG signals measured from the chest using the LIG sensors (top) and conventional gel electrodes (bottom). **Reprinted from** [78] **with permission from Advanced Materials Technologies– Wiley Online Library.**

A recent study reported a method to transfer the LIG on PI to elastomer/ sugar-based composites. Upon dissolution of sugar, these sugar-based composites yield elastic bioelectronic sensors [78]. Fig. 1.10 shows the placement of these sensors at different spots on the body to test skin hydration and temperature levels, which can be used to assess the physical and physiological condition of a human being. This combined with the electrical conductivity of porous LIG structure enables the use of these bioelectronic sensors to measure ECG, hydration and temperature responses on the skin of the subject being tested. The resistance changes upon stretching and bending and as a function of temperature which helps record ECG and temperature signals. These sensors exhibited a high gauge factor of 37 and pressure sensitivity of 0.088 kPa^{-1}.

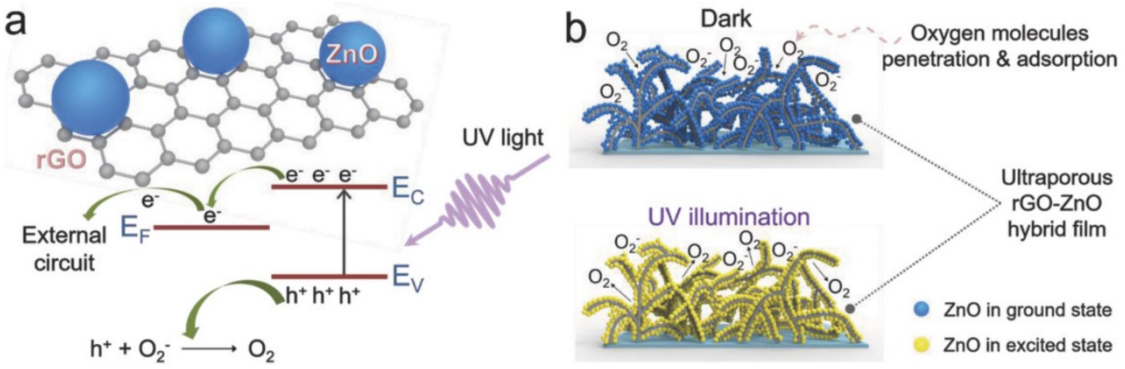

Figure 1.11: Photoresponse mechanism of the ultraporous all rGO–ZnO photodetector. a) Energy band diagram of the rGO–ZnO hybrid. EC and EV represent the conduction band and valence band of ZnO, respectively; EF represents the Fermi level of rGO. b) Schematic model of the photodetection mechanism of the 3D ultraporous rGO–ZnO hybrid film. **Reproduced from** [79] **under the Creative Common – BY license.**

A recent work reported adjusting photon density via the modulation of a femtosecond laser, rGO-ZnO hybrid nanocomposites composites were demonstrated with tuneable electronic and optoelectronic properties[79]. The pulse duration and peak power of the laser ensured the reduction of GO to rGO to form ZnO composites while not ablating the substrate.

Lasing at slower and faster speeds is used for fabricating the active detection layer and the electrodes respectively. As seen in Fig. 1.11, the rGO flakes are anchored to the substrate with poorly crystalline Zno Nanoparticles which facilitates current delivery to the external circuit. ZnO rises to an active state upon irradiation with UV radiation.

1.4 Outline of the thesis

Graphene has created significant research interest in a variety of fields due to its attractive properties. Graphene production methods are improving every year and new techniques like laser induction are being explored to effectively utilize the material's property for diverse applications. Research on LIG produced on environment friendly substrates is scarce and the substrates used are also rigid in nature. Due to rising environmental concerns and physical limitations of a rigid substrate, there is a need of eco-friendly stretchable/-flexible materials that can be employed to utilize LIG on a large scale. Lignin in a polymer matrix serves as the perfect choice for such a substrate that is inexpensive, eco-friendly and physically versatile to be used for various applications. Further, the LIG produced in our study exhibits low resistance which is used to create a pressure sensor to show its applicability.

The thesis is divided into three chapters. Chapter 1 introduces the material - graphene. Then, a literature survey is done to give an overview of graphene, elaborating on material properties and different methods of manufacturing. It then elaborates on LIG, focusing on its properties and various applications. The section ends by outlining the motivations and contributions of the thesis work.

Chapter 2 is dedicated towards utilizing the natural polymer lignin to obtain graphene via laser induction. This biopolymer is derived from wood and was claimed in previous reports to be the primary contributor towards the production of graphene on wooden substrates like paper, cloth etc using a process called laser induction. A thin film fabricated solely by mixing this biopolymer with PDMS, can give a substrate to produce LIG that is stretchable, sustainable and inexpensive. This thin film is named lignin in PDMS matrix (LIPM). Further, a description on the laser induction process to produce graphene on this stretchable film and further characterization of the LIG produced has been given.

Chapter 3 explains the utilization of LIG on LIPM films towards pressure sensing. There is a brief background on pressure sensors and the scientific mechanisms employed in these pressure sensors. After elaborating the fabrication methods and characterization of the sensor, the chapter concludes with a discussion of the hypothesis on the working mechanism behind the LIG on LIPM film based pressure sensors.

Chapter 4 concludes the thesis with a discussion about the future works associated with LIG on LIPM films, including changing fabrication environment to improve LIG quality and exploring new applications to exploit the properties of LIG on LIPM films.

Chapter 2

Fabrication of laser-induced graphene onto lignin-upgraded polymer matrix

2.1 Introduction to lignin

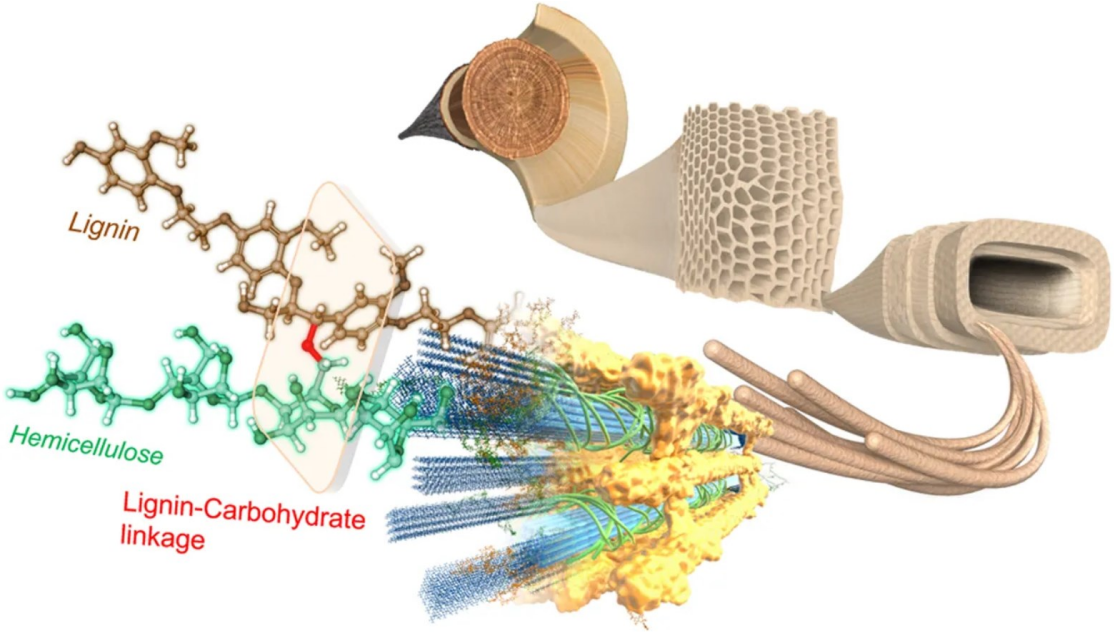

Figure 2.1: Breakdown of wood into its composites (cellulose, hemicellulose and lignin). As can be seen the cell-wall comprises of the two major composites, lignin and hemicellulose, that crosslink with each other to form fibril structures that facilitate the strength of the cell wall. **Reprinted from** [80] **under the Creative Commons - BY License.**

Wood is a biopolymer composite which exhibits large structural complexity. The diverse species of wood further add to the variability found between in different structures across the species. The nanostructure of wood cell walls comprises three biopolymers: cellulose, semicrystalline fibrils that serve as the elementary structure in wood; hemicellulose cross-links these elementary fibrils while facilitating interaction between the biopolymers; and

lignin, an amorphous polymer of phenylpropanoids that forms in close association with hemicellulose.

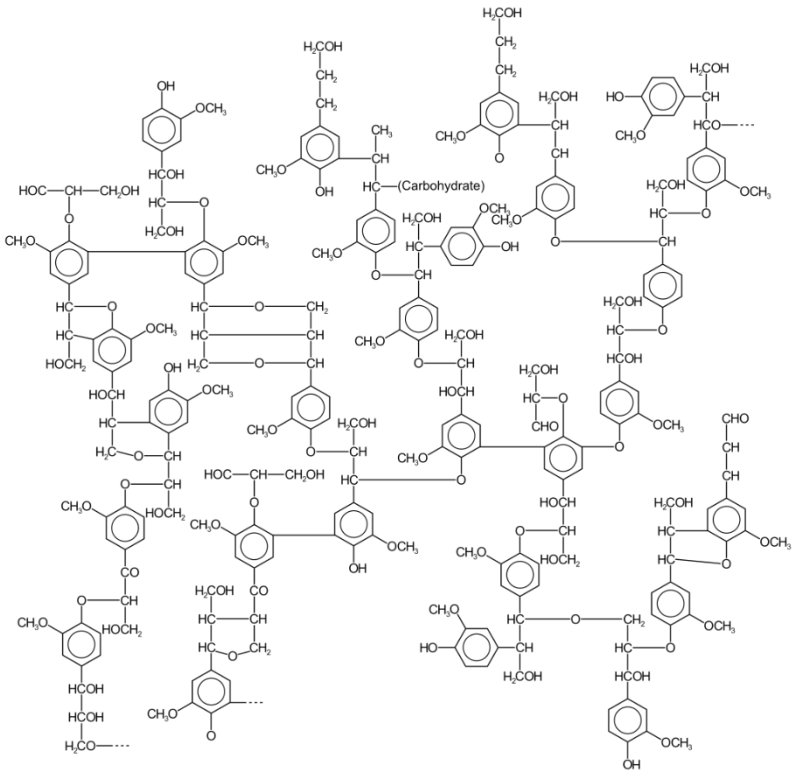

Figure 2.2: Chemical structure of lignin with a variety of phenylpropanoid structures forming ether (C-O) and condensed (C-C) linkages with each other. **Reprinted from [81] under the Creative Commons - BY License.**

Lignin is a highly complex biopolymer found in both softwood and hardwood. Its complex structure is an odd occurrence among other natural biopolymers. The lignin structure can be classified into three primary monomers or monolignols[82]: p-hydroxyphenyl (p-coumaryl alcohol), guaiacyl (4-hydroxy-3-methoxyphenyl, coniferyl alcohol) and syringyl (3,5-dimethoxy-4-hydroxyphenyl, Sinapyl alcohol) depending on the wood species [83,84,85]. These monomers are connected via various ether linkages (C-O) and condensed (C-C) bonds which leads to lignin's heterogeneous chemical structure. The lignin polymer is neither cross-linked nor unbranched linear nor linear with side chains hence it can be network of the monomers. It does not have a well-defined primary structure. Softwood has a higher proportion

of Guacil units and a small proportion of p-hydroxyphenyl units whereas hardwood mostly comprises of Guacil and Syringyl units. Lignin is synthesized by a radical polymerization process without catalysts unlike other biopolymers which undergo controlled condensation inside an enzyme complex [86]. There is extensive debate around catalysis with some studies suggesting special direction sites in the cell wall that could catalyse the coupling [87]. There are differences in lignin structure between different types of cells. Hardwood cells generally have more coniferyl alcohol and condensed bonds than libriform fibers. In softwoods, the wood lignins contain considerable amounts of p-hydroxy coumaryl alcohol and are more condensed, hence they possess a more resistant structure.

2.2 LIG production using lignin-upgraded polymer matrix

A recent study done in 2017 determined that higher lignin content in wooden substrates used for LIG production gave higher quality graphene [49]. Hence substrates such as pine with higher lignin content created better quality graphene as compared to birch and oak substrates with lower lignin content. The laser induction process requires hard substrates or films upon which the laser beam can be traced to produce LIG. Plain lignin powder is not a fit substrate to produce LIG and must be brought to a stable form for laser induction. Suspending lignin in a polymer matrix to create robust film was the best way to ensure uniform distribution of the lignin molecules that could be utilized for various purposes.

2.2.1 Fabrication of lignin in polymer matrix (LIPM) films

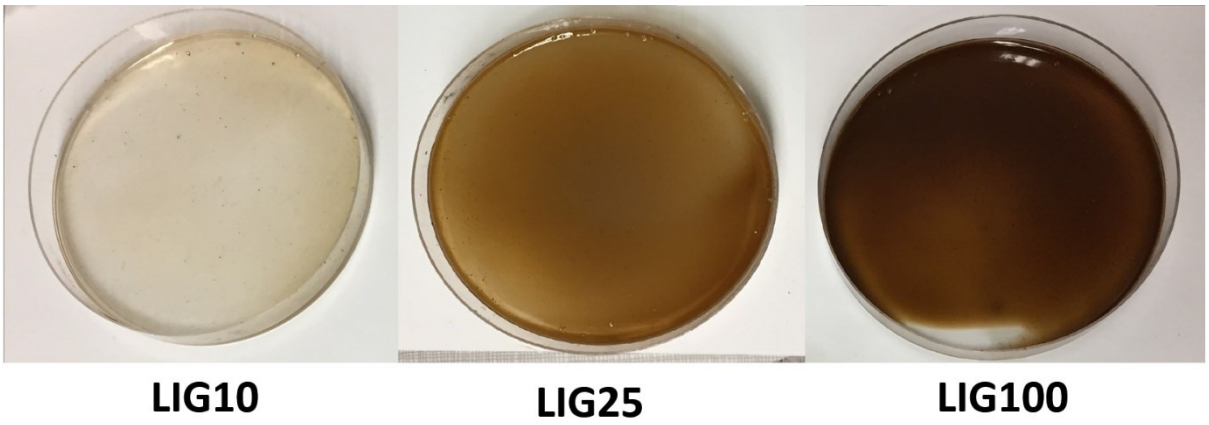

Figure 2.3: The photographs show the 3 LIPM films (LIG10, LIG25 and LIG100) with 0.41 wt%, 1.0 wt% and 4.0 wt% of lignin in PDMS. Lignin concentration is visibly changing the colour of the LIPM

As discussed in the introduction to this section, we created a suspension of lignin in polydimethylsiloxane (PDMS) which is a synthetic polymer. Three different mass fractions: 0.41 wt%, 1.0 wt% and 4.0 wt% of lignin in PDMS referred to as LIG10, LIG25, LIG100 respectively, thus created a Lignin in Polymer Matrix (LIPM) film as observed in Fig. 2.3. These three LIPM films with different mass fractions of lignin were then utilized to produce LIG via the laser induction process. It can also be observed in Fig. 2.3 that lignin concentration severely altered the colour composition of LIPM films. Upon observation if was seen that change in lignin concentration also led to different mechanical properties, with LIG100 being the most stretchable film, however the mechanical properties of these films were not characterized in this work.

2.2.2 Laser induction mechanism of LIG production using LIPM films

There were two studies done using the laser induction process to understand the properties of the LIG produced on LIPM films. In the first study, laser induction was done in a pattern as seen in Fig. 2.4b on each of the LIG10, LIG25 and LIG100 films. This was done to ascertain the relationship between lignin concentration and quality of graphene produced. In the second study, the laser induction was done by varying the trace speed of the laser in order to judge the most suitable laser tracing speed to produce the highest quality graphene. The commercial scribing laser employed for these studies has a fixed power and focal length; hence the laser trace speed is the only variable for modulating the effective laser dose – energy transfer onto LIG25 films. The results for both these studies were characterized using Raman spectroscopy, while scanning electron microscopy (SEM) and resistance measurements were also used in the second study to critique the structure and resistance of the different LIG samples respectively as discussed in detail in Section 2.2.3. The schematic in Fig. 2.4a shows the laser induction process employed to create LIG traces ion LIPM films, the real image of which is seen in Fig. 2.4b.

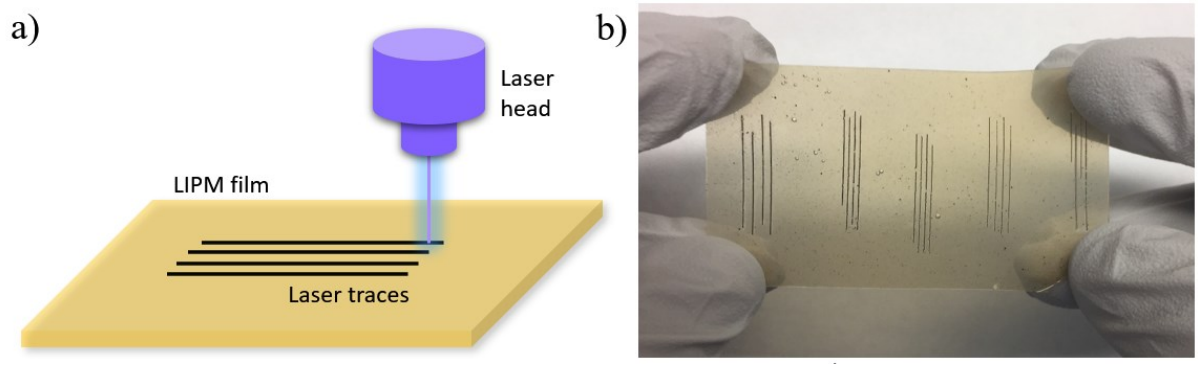

Figure 2.4: (a) The schematic shows the laser induction process on the LIPM film. (b) Image of the LIG traces on the LIPM (LIG25) film.

This laser-induced conversion process of aromatic molecules to graphitic structures is unclear in literature; it is argued that lasing at higher wavelengths leads to photothermal ablation [41] while lasing at lower wavelengths leads to photochemical degradation via direct bond breaking [41] of aromatic molecules to graphitic structures. If argued that laser wavelengths centred around UV (~305nm) lead to only photochemical bond breaking[88], it should be noted that the lignin concentration in PDMS would be the only limiting factor for LIG (due to limited surface area of exposure to the laser beam)[41], but for our tests, varying the laser speed also gave different I_D: I_G ratios for samples with a constant wt% of lignin indicating a more nuanced process (including photothermal degradation) at work. Here, we posit that the 410 nm laser causes the degradation of the substrate via both photochemical and thermal pathways as discussed in the following.

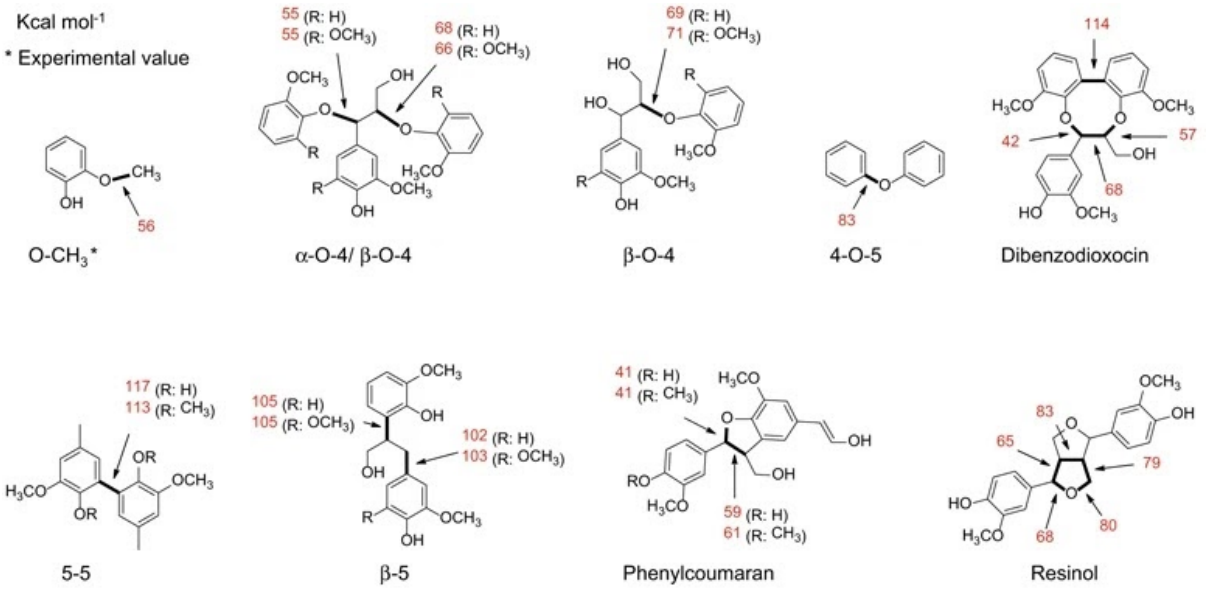

Figure 2.5: Bond enthalpies of the various organic linkages in the lignin structure (kcal.mol^{-1}) [84].

Lignin's degradation to LIG can be studied by examining bond enthalpies and pyrolysis pathways of the lignin structure. Pyrolysis can be defined as thermal degradation under a limited amount of oxygen. Research on lignin pyrolysis pathways has been mostly done using highly simplified models that do not represent lignin's structure[89]. Phenolic moieties are the most abundant aromatic species present in the lignin structure contributing toward porous graphitic structures [88] [89]. Fig. 2.5 shows the variety of bond enthalpies of different linkages in the lignin structure. The photon energy of the laser at 410 nm is ~3.02 eV or 69.64 kCal.mol^{-1} which can directly (photochemically) break most phenolic bonds with hydrocarbon moieties having bond dissociation enthalpies in the range 40-80 kCal.mol^{-1} (Fig. 2.5), liberating small organic by-products[90]. Few direct bonds between aromatic linkages have high bond dissociation enthalpies around 100-120 kCal.mol^{-1} as seen in Fig. 2.5, which prevents photochemical action and preserves the direct chain linkages between aromatic structures contributing towards the formation of honeycomb like graphitic structures [84,90]. However, excess high energy photons delocalize the electrons in the aromatic structures called 'chromophores' in [91], resulting in more collisions causing vibrational states, which coupled with the heat from photochemical bond breaking [88,92] leads to further thermal ablation of the nearby regions. Hence, I posit that both photochemical and photothermal processes lead to the formation of LIG on LIPM substrates.

2.2.3 Characterization of LIG produced on LIPM films

In the two laser induction studies, altering lignin concentration and laser trace speed respectively produced effects on LIG structures which were systematically analysed.

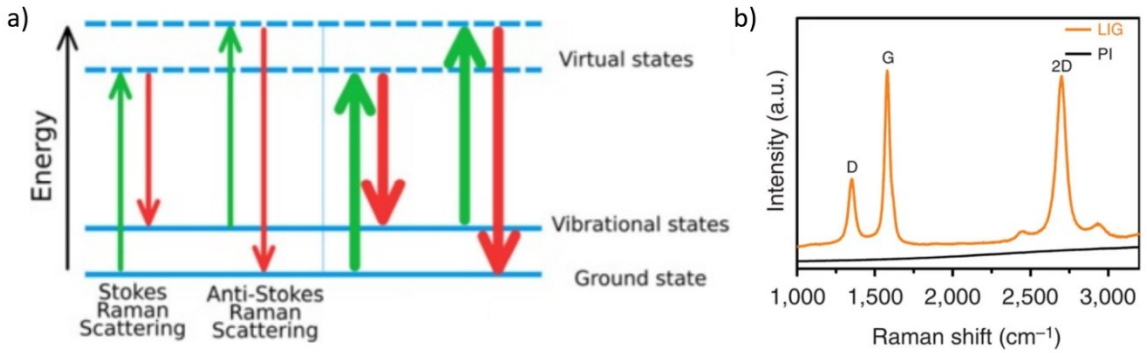

Figure 2.6: (a) Stokes and Anti- Stokes lines **Reproduced from** [93] **under the Creative Common – BY license.** (b) Raman spectrum of laser induced graphene with its characteristic D, G and 2D peaks. **Reprinted from** [42] **with permission from Nature Communications.**

Raman spectroscopy is a technique used to characterize and often confirm the presence of graphene after laser induction on a sample. Raman spectroscopy measures the change in the polarizability 'α' of a molecule using when an electron transitions from a lower energy state to a higher energy virtual state and back to a another lower energy state causing a stokes shift, which can be used to identify any unknown molecules in a given sample. As shown in Fig. 2.6a stokes shift can be of two types: transition from an excited virtual state to an energy state lower than (Anti-Stokes Shift) or higher than (Stokes Shift) the original energy state. These shifts are characteristic to different molecules and are hence used for identification purposes. The observation of the Raman spectra of the sample after the laser induction process can be used to determine the presence of graphene due to the presence of graphene's characteristic peaks as seen in Fig. 2.6b. The peaks in Fig. 2.6b at 1350 cm^{-1}, 1580 cm^{-1} and 2700 cm^{-1} are respectively referred to as the I_D, I_G and I_{2D} peaks [94] and they confirm the presence of multi-layer graphene (MLG). Different structural properties of graphene can be ascertained from these Raman peaks.

The D peak stands for the disorder in the sp^2 hybridized structure of carbons in graphene and 2D peak indicates the formation of multi-layered graphene[95,94]. The full-width at half maximum (FWHM) of the 2D peak also carries information about graphene. A wider FWHM in the Raman spectra of graphene signifies a larger number of layers in the graphene like structure. For pristine single-layer graphene (SLG), the FWHM has the least value which increases with the additional layers of graphene[104]. The ratios I_D: I_G and I_{2D}: I_G from the Raman spectrum, indicate the amount of disorder and presence of multiple graphitic layers in the LIG.

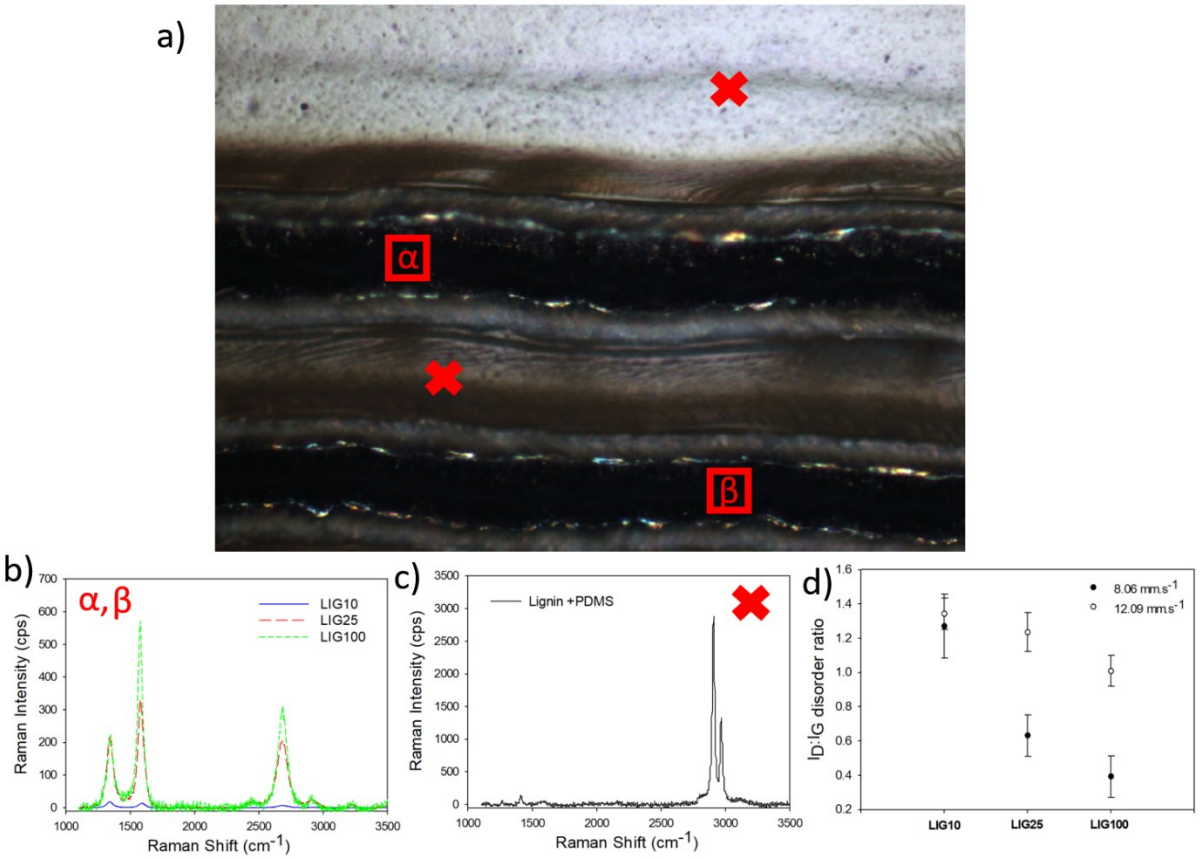

Figure 2.7: LIG on LIPM films. (a) Optical image of the lased lines depicting the lased region and the surrounding regions on one of the LIPM films (LIG25). (b) The Raman spectra of the lased area (marked with '**α**' and '**β**' in the image) on different LIPMs (LIG10, LIG25, LIG100), showing G(~1580 cm^{-1}) and D(~1350 cm^{-1}) peaks where laser tracing occurred in contrast to (c) peaks (~2905 cm^{-1} and ~2965 cm^{-1}) of the background LIPM film (marked with '**X**'). d) The change in I_G:I_D ratios with increasing trace speed. The images were taken on the Nicolet Omega Microscope using a 10x 0.25 BD objective.

As discussed in the previous section 2.2.2, the first study focused on the relationship between lignin concentration and graphene quality. Hence, the three LIPM films with different lignin concentration were lased and characterized for the presence and quality of graphene. The lasing was done at only two speeds to observe whether there was a linear relationship between the quality of graphene produced and different concentrations of lignin across two different laser trace speeds as well.

Fig. 2.7a shows a visual image of LIG produced on the LIG25 film. As seen in Fig. 2.7a, the middle of lased paths/ regions are marked with 'α' and 'β' and regions with 'X' mark the background of the substrate, to contrast between the lased an background regions for all LIPM films with different concentrations. Fig. 2.7b indicates the Raman spectra associated with the α and β regions marked in Fig. 2.7a. The Raman spectra of the 'α' and 'β' in Fig. 2.7b shows three prominent Raman peaks: the G peak (~1580 cm^{-1}), D peak (~1350 cm^{-1}) and 2D peak (~2700 cm^{-1}), confirming the presence of MLG in the LIG obtained from LIPM films. This can be contrasted with the Raman spectra (Fig. 2.7b) of the background regions marked in 'X', where the only prominent peaks are at ~2940.5 cm^{-1} and ~2890.5 cm^{-1} belonging to the asymmetric and symmetric stretches respectively, of the CH_3 molecule in PDMS[96]. It should also be noted that lasing a pure PDMS film did not affect the film, leaving it perceivably untouched. This implies lignin is the sole contributor of graphene in LIG because lignin's structure comprises of three primary precursors or monolignols as mentioned in section 2.1: *p-coumaryl alcohol*, *coniferyl alcohol* and *sinapyl alcohol*, all of which have aromatic residues which contribute towards the formation of graphitic structures in LIG[92,84]. There is also visible soot deposition in Fig. 2.7a near the lased path, caused by formation of gaseous by-products from the lasing action, which was found to be lower at higher speeds, but these soot depositions however, show no significant peaks in Raman spectrum other than those similar to those obtained for pure PDMS. Hence, it is understood that PDMS with its two cis- and trans-

methyl groups attached to a Si atom, occurring in a repeating polymeric chain, has no contribution towards LIG as these methyl groups are unable to form aromatic structures. Hence, the Raman spectra in Fig. 2.7a obtained for different LIPM films confirms a linear relationship between lignin concentration and graphene quality. The data in Fig. 2.7c shows further proof of this linear relationship that extends across different laser speeds (12.09 mm·s^{-1}) as well, concluding that higher lignin concentrations give lower I_D:I_G ratios implying LIG quality is LIG100> LIG25> LIG10 or that LIG100 has the least structural defects for a given laser speed.

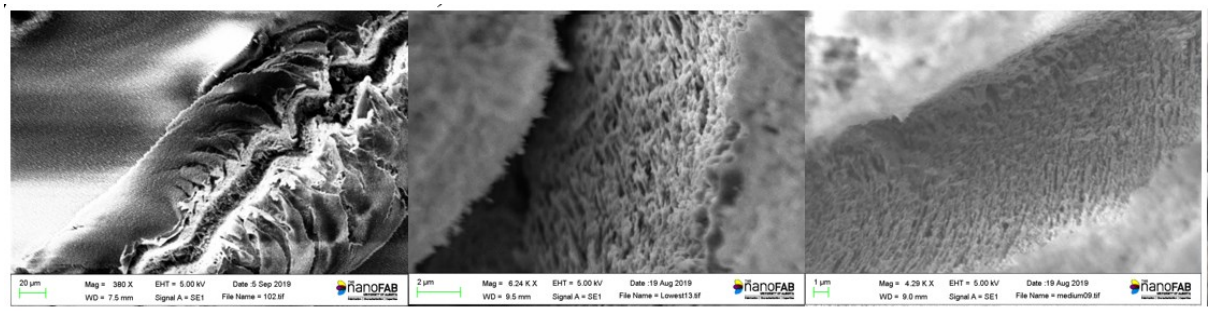

Figure 2.8: SEM images (a) of the laser trace 8.06 mm.s^{-1}, (b) and (c) are magnified images of the porous LIG on the LIPM film surface at 8.06 mm.s^{-1} and 12.09 mm.s^{-1} respectively. Images were taken on the Zeiss Evo M10 SEM.

In the second laser induction study, the median value of the weight fraction, the LIG25 film was chosen to test the performance of different laser trace speeds to ascertain the relationship between laser trace speed and graphene quality and possibly identify an optimum speed to maximize graphene quality. Seven different laser trace speeds were programmed to ascertain the optimum speed that would produce the highest quality graphene. Fig. 2.8 shows the SEM images that were taken for the two different speeds (8.06 mm·s^{-1} and 12.09 mm·s^{-1}) chosen from near the median of the 7 different speeds. It is clearly noticed that LIG is produced in a porous structure and that the porosity of these structures changes with laser trace speed. Here, larger pores and flakes have formed at the lower speed of 8.06 mm·s^{-1} indicating better quality, because larger flakes of graphene are desirable as seen in Section 1.2. Characterizing

the LIG obtained with different laser trace speeds using Raman spectroscopy reveals interesting results.

Fig. 2.9a extends the analysis in Fig. 2.7c by showing an improving trend in I_D:I_G and I_{2D}:I_G ratios with a larger range of trace speeds. Also, a steady rise in I_{2D}: I_G ratios indicate formation of a higher number of graphitic layers, that also have fewer defects (I_D: I_G ratios) in the porous graphene structure[95]. This further confirms the contribution of photothermal conversion, since if the mechanism only comprised of direct bond breaking, different laser trace speeds would have given very similar I_{2D}:I_G ratios on the same wt% samples.

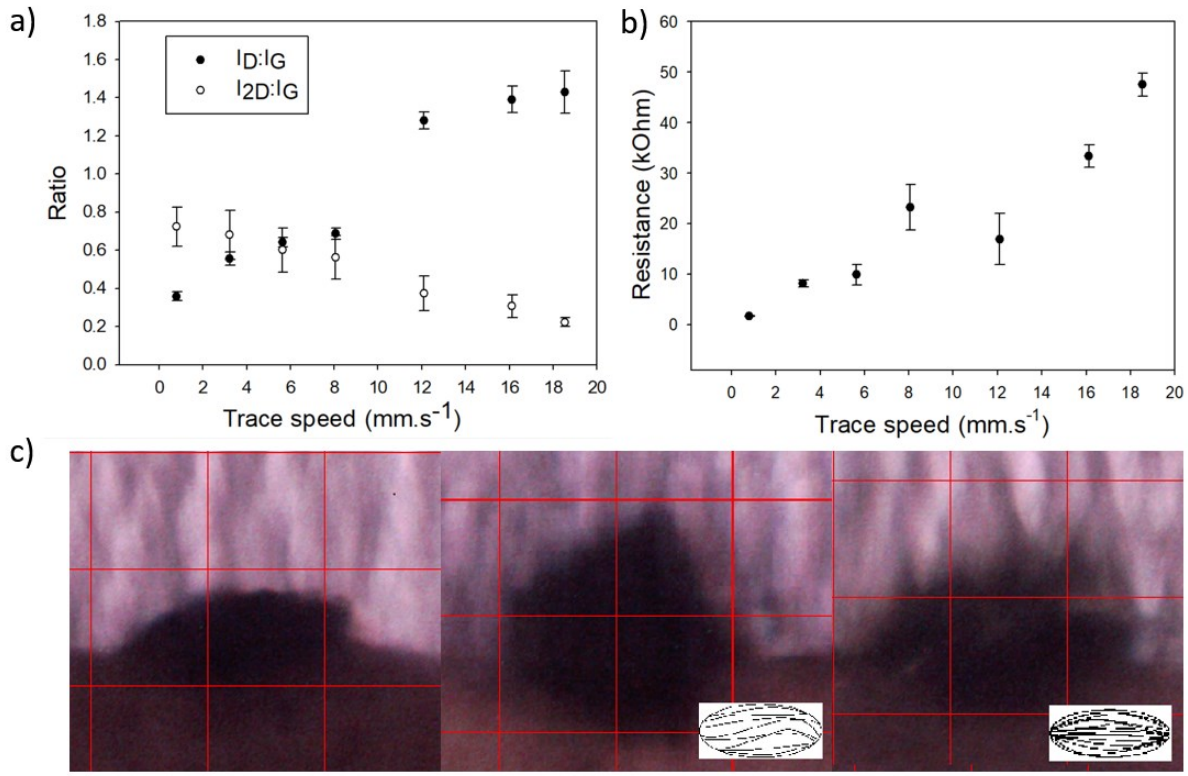

Figure 2.9: a) Disorder ratios. b) Trend in resistance. c) Trend of porous cross-section - the 3D porous LIG structure's cross-sectional variation for trace speeds (i) 12.09 mm·s^{-1} (left), (ii) 8.08 mm·s^{-1} and (iii) 5.64 mm·s^{-1} (right) with the insets in (ii), (iii) showing porous cross section. The image was taken on the OMAX A3550U3 Optical Microscope with a 10x/0.25 objective.

Resistance measurements in Fig. 2.9b show decreasing resistance of LIG with slower trace speeds in accordance with the data (Fig. 2.9a) on consistently improving I_D: I_G ratios (higher quality LIG) with slower trace speeds. The trend in resistance of LIG shown in Fig. 2.9c indicates similar values for all speeds with a slight deviation at the speed of 8.06 mm·s^{-1} as explained below.

Visual observation while laser tracing on LIPM films shows evolution of gaseous by-products for a limited time duration at a given lased spot. Gaseous evolution starts at a trace speed of 12.09 mm·s^{-1} going towards lower trace speeds, with minimal to no evolution at speeds higher than 12.09 mm·s^{-1}. At higher speeds, there is no gaseous evolution due to shorter heat accumulation time but at lower speeds, due to longer heat accumulation time, heat left after the gaseous evolution is over, will allow porous LIG to settle into low porosity structures because there are no gases are evolving to push against the porous walls. The point of inflection where evolution of gaseous by-products still occurs when most heat has dissipated, leads towards a high cross-section porous structure due to rapidly evolving gases. To further confirm this, as discussed at the end of section 2.2.2, longer duration for heat accumulation enables the graphitic structures to settle into uniform porous 3D structures, which is imitated by the data in Fig. 2.9a that shows lower speeds have lower disorder (I_D: I_G). This point of inflection is observed in the image shown in Fig. 2.9c-(ii) where the cross-section (highly porous structure) is highest at 8.06 mm/s. Also observed in Fig. 2.9a, the I_{2D}: I_G ratios depict the number of layers has not radically increased indicating high porosity at 8.06 mm·s^{-1}. Larger porosity implies fewer deformed LIG layers (I_{2D}: I_G) are close to each other with hindered electron conduction pathways compared to lower porosity LIG with high I_{2D}: I_G. This fact coupled with the formula used for resistivity, $\rho = RA/L$, which is unable to account for a porous cross section over a solid cross section, brings about a single large peak in resistivity, which is otherwise almost constant. Here, for the LIG on LIG25 LIPM films, the resistance (R) LIG varies from 1.7 kΩ to 47.5 kΩ

(as seen in Fig. 2.9a) while the area of cross-section (A) varies from 0.1 to 0.09 mm^2 for trace speeds of 0.8 $mm \cdot s^{-1}$ to 18.5 $mm \cdot s^{-1}$ respectively, where the length (L) of the LIG remained a constant of 1.2 cm.

2.3 Experimental details

This section provides the details of techniques and tools employed to produce LIG on LIPM substrates. The process to fabricate thin LIPM films from lignin and PDMS is described followed by the information on the laser system and the settings used for the lasing process. The section concludes with detailed characterization and analysis techniques used on the LIG samples.

2.3.1 Preparation of LIPM films

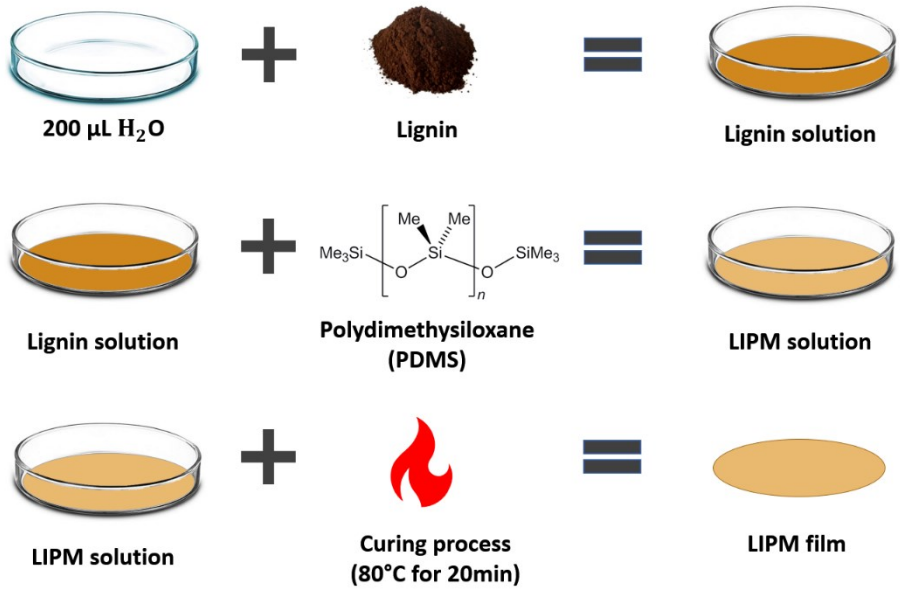

Figure 2.10: Schematic showing the fabrication process for LIPM films.

Three different concentrations of lignin were tested to assess the relation between lignin concentration and the quality of graphene produced. We separately dissolved 10 g, 25 g, 100 g of lignin in 200 µL of deionized (DI) water to improve the miscibility of lignin. 200 µL of water would eventually evaporate upon the curing process hence it was not considered for calculations. After mixing the respective concentrations of lignin in DI water with a spatula, 2.5 mL of PDMS polymer was prepared by further adding the PDMS base and curing agent in a 10:1 ratio to the lignin and DI water mixture. A thorough mixing process using a clean spatula is performed until the suspension has a uniform light brown colour as shown in Fig. 2.10 and Fig. 2.3. This is followed by a polymer curing process for a duration of 15 min on a hotplate at 80°C, where the temperature was monitored using a laser temperature scanner. At the end of the curing process, three different LIPM films - LIG10, LIG25, LIG100 representing 0.41 wt%, 1.0 wt% and 4.0 wt% lignin in PDMS respectively, had been fabricated.

2.3.2 Experimental setup of the laser

An inhouse laser from a Winbo™ 3D printer was employed for the lasing process to produce LIG on the LIPM substrates. This laser was centred at a wavelength of ~410 nm as seen in Fig. 2.11, which depicts the central wavelength of the laser as measured using THORLabs™ photodiode and Oceanview™ software. As previously discussed, the 3D printer laser in our study was a continuous wave visible laser operating at a wavelength of 410 nm. The spot size of the laser could not be computed due to limited availability of resources but could be approximated to ~100 µm in diameter. The power of the laser is approximately 630 mW, which is focused upon a circular area with radius ~50 µm and this gives a laser intensity of ~8×10^7 $W \cdot m^{-2}$ at the focus point. The intensity of the small peaks in Fig. 2.11 is very small relative to the 410 nm peak which saturates the photodiode. The laser height could be adjusted in steps of 1 mm and was visually adjusted to sit at 47 mm above the lasing tracing surface

using a height setting knob on the 3D printer to provide the best focus. Winlaser was the laser printer software used to compile the *.gcode* files, which were then uploaded onto the laser using a memory card. For characterization, the laser was set to trace only 4 parallel lines well separated from each other, this allowed for characterization of graphene obtained using a single laser trace and also helped with redundancy during the characterization phase due to the fragile nature of LIG. The distance between the trace lines matters as placing these trace lines closer to each causes overlap in the lased regions making it difficult to observe and analyse the characteristics of graphene produced both visually and spectroscopically.

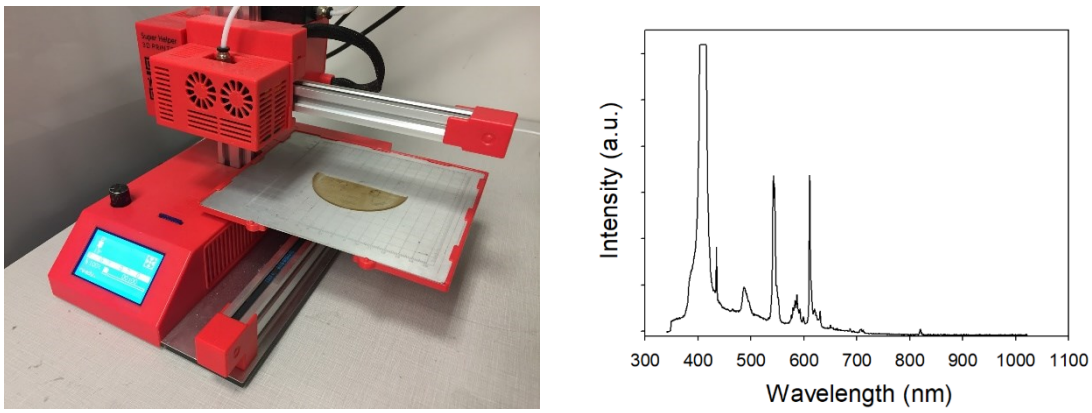

Figure 2.11: Photograph showing the Winbo™ 3D printer, in which the laser is present inside the module pointed out. The knob next to the screen was used to control the laser settings and select the laser code to be used. (b) The frequency spectrum of the laser measured using a photodiode has been shown. The dominant peak which saturated the sensor was at ~410 nm, the other peaks have a relatively very small intensity.

For the first study, the 4-line laser tracing was done separately on each of the LIG10, LIG25 and LIG100 LIPM films. For the second study however, the film LIG25 was selected as the sample with median mass fraction to run the laser trace speed tests. The *.gcode* file was used to program 7 different speeds: .80 $mm \cdot s^{-1}$, 3.22 $mm \cdot s^{-1}$, 5.64 $mm \cdot s^{-1}$, 8.06 $mm \cdot s^{-1}$, 12.09 $mm \cdot s^{-1}$, 16.12 $mm \cdot s^{-1}$, 18.54 $mm \cdot s^{-1}$ for laser tracing onto the LIG25 film. Four lines of each speed were used to improve the redundancy of the samples.

2.3.3 Characterization tools – Raman spectroscope

There were several tools used for characterizing the LIG samples produced on LIPM films. Raman microscopy was the primary tool used to characterize the quality of graphene produced as it gave an accurate study on the LIG's physical structure. We also used the Keithley(R) Sourcemeter 2400 to make resistance measurements.

The samples to be analysed by Raman spectroscopy were carefully transferred on a glass slide and then mounted onto the glass slide holder inside the Nicolet Omega XR Raman Microscope with an operating wavelength set at 532 nm. The objective used for capturing the image was set to a focus of 10x using a 0.25 BD objective.

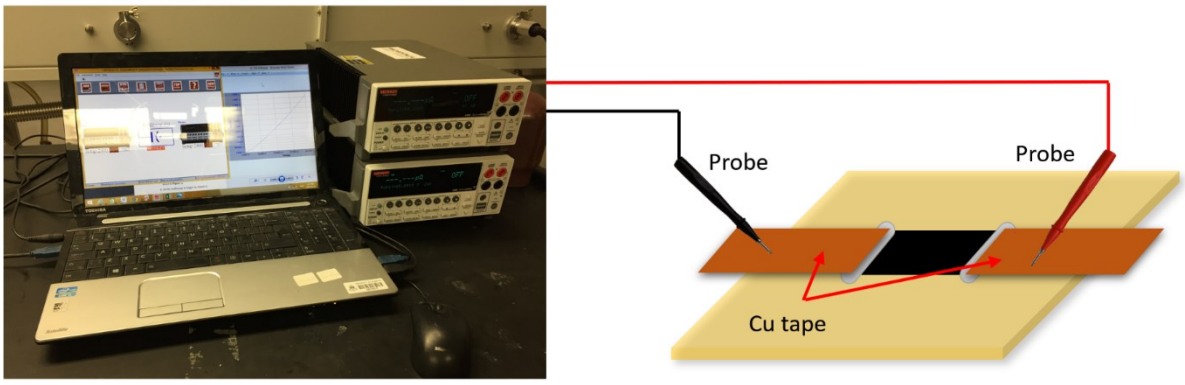

Figure 2.12: The photograph schematic shows the electrical connections that were made while making the resistance measurements.

The Keithley Sourcemeter 2400 was connected to a laptop via a USB cable and was set to operate and measure the current characteristics across the two probes using a voltage sweep as shown in Fig. 2.12. The voltage was given across two probes, which could not be directly connected to graphene due to improper and unstable contact, since LIG cannot support the mechanical strain produced by the weight of the probes. For this reason, a copper (Cu) tape was utilized to provide a conductive medium of transition with a large surface area to serve as

an electrical contact for the probe and the LIG sample. As mentioned in Section 2.3.2, multiple laser traced LIG lines were used to improve the redundancy of the samples, the Cu tape was also able to establish electrical contact with all 4 lines of LIG. Silver (Ag) paste further helped create an electric contact between the LIG lines and the copper tape reducing contact resistance. The Ag paste was cured at room temperature for 24 hrs. The I-V characteristics of the measurements were used to obtain the slope and hence the resistance of the sample. The resistance obtained via this method was for the 4 laser lines in parallel, hence the resistance observed on the slope was divided by 4 to obtain the actual resistance value of the sample.

2.4 Summary

Graphene production is a time-consuming process that requires the use of sophisticated tools and chemical resources that all add towards the production cost. Laser induction techniques for producing graphene have the potential for low-cost mass production. Our work has shown that lignin, a composite of wood which is an inexpensive renewable resource, can be utilized to produce graphene on a stretchable/flexible film in a one step process.

We have fabricated an environment friendly, stretchable substrate and demonstrated a method to produce high quality LIG. The theory to elucidate the effect of minimal addition of lignin and the optimization of laser trace speed on improving LIG quality has been presented. It is supported by characterizations through Raman spectroscopy and conductivity measurements that show how lower structural defects are observed with higher lignin concentrations and slower trace speeds, where LIG as a pressure sensor is used to serve as an example of a flexible electronic application. The use of lignin and a commercially available laser shows the eco-friendly nature and wide applicability of discussed LIG technique.

The optimum-quality LIG obtained in our work has the lowest resistivity of ~10^{-2} Ω·m. This resistivity value enables the use of LIG for sensor-based applications. The practical consideration exploited in our work refers to the use of the LIG produced as a pressure sensor that senses a change in the resistance of the sample to identify the presence of an object atop the sensor.

Chapter 3

Flexible pressure sensors employing laser-induced graphene

3.1 Introduction to pressure sensors

Pressure (P) in a system is defined by force applied per unit area: $P = F/A$ where F is the force applied in Newtons and A is the area in meter sq. onto which the force has been applied. A pressure sensor is a device that can measure an applied force on a given area in a solid, liquid or gaseous medium. This sensor works as a transducer that generates a signal as a function of an applied mechanical force. An electronic pressure sensor translates mechanical force into an electrical signal which can be used to control or monitor an application or a system respectively.

3.1.1 Pressure measurements

There are various kinds of pressure measurements that can be classified into categories, related to either the purpose or method of operation.

Absolute pressure sensor - This sensor senses pressure changes relative to a reference chamber (near vacuum). Gauge pressure sensor - These sensors measure the pressure change relative to atmospheric pressure. A measurement of 0 on these sensors implies atmospheric pressure. Vacuum pressure sensor - This sensor measures the difference in pressure below the

atmospheric pressure level i.e. giving the difference between the low pressure and the atmospheric pressure. It can also be used for measuring absolute pressure relative to vacuum. Differential pressure sensor - This is a sensor that measures the difference between two different pressures at either side of the sensor. Most pressure sensors are technically differential pressure sensors; for example, a gauge sensor is a differential pressure sensor with one end open to measure the ambient atmospheric pressure. Sealed pressure sensor - This pressure sensor is similar to the gauge pressure sensor but measures the pressure relative to a fixed value and not atmospheric pressure.

3.1.2 Types of pressure sensors

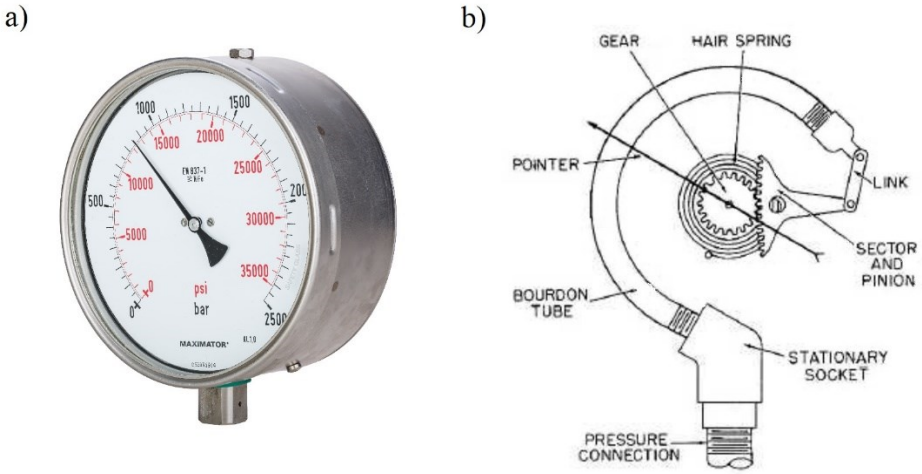

Figure 3.1: (a) A classic bourdon tube pressure gauge which is a force collector type pressure sensor. (b) The schematic of the bourdon tube gauge that pivots the pointer using a gear mechanism (tooth quadrant) which is pushed by an increasing pressure at the linkage. **Reprinted from [97] under the Creative Commons - BY License. Reprinted from [98] with permission from Intrumentationtools.com.**

There are two common types of pressure sensors: First, force collector type: This sensor employs a force collector such as a piston, diaphragm, bourdon tube etc. to measure the strain

(or deflection) by a force over an area. Second, other types of electronic pressure sensors that use density among other properties to detect the pressure of a gas or liquid.

Force collector type

Strain gauge - This type of a pressure sensor, is usually operated in a Wheatstone bridge configuration with foil or silicon strain gauges as the circuit elements. Generally, a diaphragm is used as the measuring element. The signal generated is then measured, amplified and conditioned by the Wheatstone bridge circuit to provide a suitable transducer-voltage or transmitter-current output representative of the applied pressure. A big advantage of this monolithic can-type design are improved rigidity and the capability to measure high pressures.

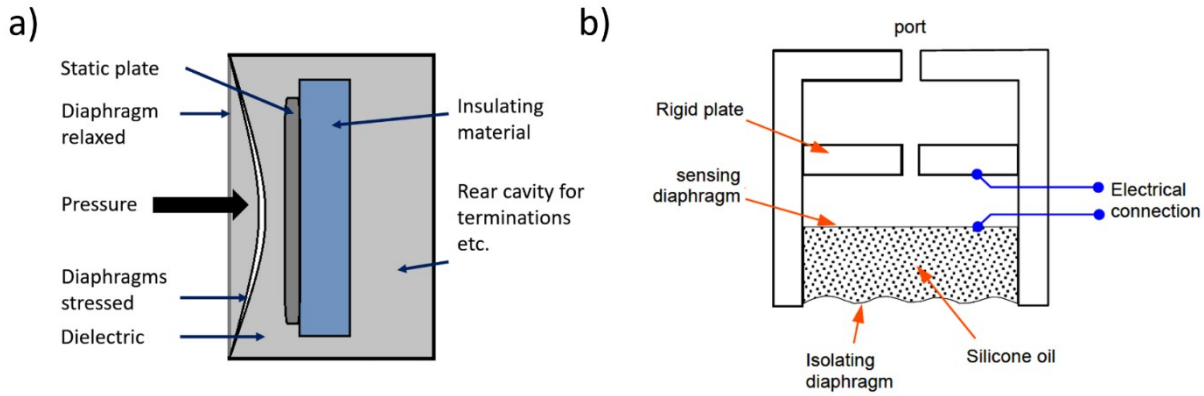

Figure 3.2: Types of capacitive pressure sensors. (a) Capacitive pressure sensor with a deflecting diaphragm causing a change in capacitance inflected by a change in the distance between electrodes. (b) Pressure on the isolating diaphragm creates a pressure differential relative to the pressure on the other end (sensing diaphragm) to cause the metal plate to deflect enabling sensing. **Reprinted from [99] with permission from Instrumentationtools.com.**

Capacitive - A capacitive pressure sensor contains a capacitor with one rigid plate and one flexible membrane which serve as the electrodes. The area of these electrodes is fixed, hence a change in capacitance is brought via a proportional change in the distance between the electrodes. The pressure to be measured is applied to the flexible-membrane side as seen in

Fig. 3.2a, and the resulting deflection causes a change in capacitance that can be measured using an electrical circuit.

Piezo-electric - These sensors measure the strain applied to a material such as quartz. Strain is applied to a diaphragm which is connected to a piezoresistive material that produces charge carriers, changing the resistance. A Wheatstone bridge senses this change and produces a dynamic electrical signal as response which can be utilized. These sensors can only be used for dynamic applications where static pressure cannot be sensed.

Electromagnetic - These pressure sensors sense the displacement of a diaphragm via inductance (reluctance), hall effect or principles of eddy current.

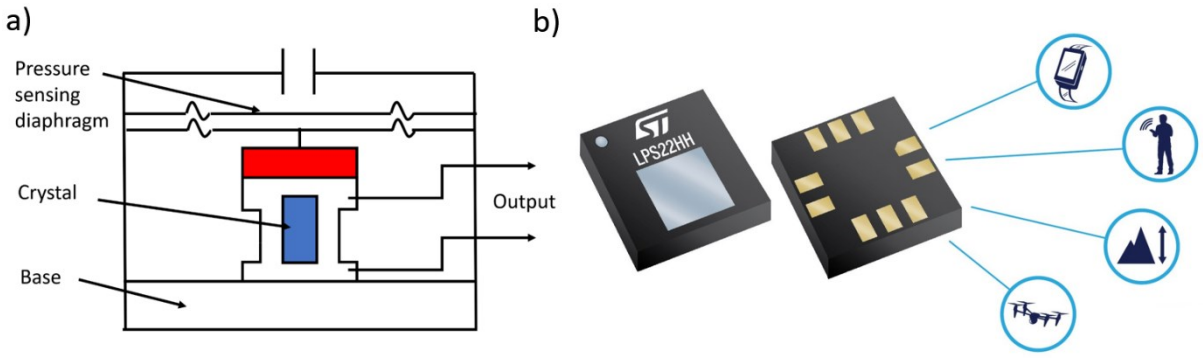

Figure 3.3: (a) A schematic showing a piezo-electric pressure sensor with a pressure sensitive diaphragm connected to the piezo-resistive crystal which would generate an electrical response proportional to the movement of the diaphragm. (b) The STMicroelectronics LPS22H MEMS piezoelectric absolute pressure sensor is a 2mm x 2mm x .75 mm MEMS device with 10 leads that can be used for applications like smartwatches, elevation sensing and drone technology. [100].

Microelectromechanical Systems (MEMS) - These sensors are relatively very small (~at the order of several 100 μm up to 2 mm) and can be manufactured on silicon, as compact surface mount devices. Since the manufacturing process occurs at the chip scale, small electronic devices like amplifiers and noise reducing circuitry can also be packed in a small

form factor with these devices which makes them very useful for various sensing applications as the outputs can be taken as both analog and digital signals depending on the associated circuitry.

Other types

Resonant - They sense a change in the resonant frequency to measure either stress or change in gaseous density caused by an applied pressure. Deployed independently, the resonating element of the sensor can be directly exposed to the media, the resonant frequency of which is based on its density. Vibrating wires, vibrating cylinders and quartz are common elements used in these sensors that provide very reliable and stable readings.

Thermal and Ionization - These sensors measure the change in density by sensing either a change in the thermal conductivity of the gas or sense a change in the flow of ionized gas particles.

As seen above, there are a wide variety of pressure sensors available. These sensors mentioned above cannot be used ubiquitously for all applications. Specific sensor requirements are given based on the application upon which the most suitable sensor is chosen. These requirements can be based on location, sensing medium, dynamic or static measurements, accuracy, size or transducing mechanism.

3.2 Fabrication and characterization of LIPM-based pressure sensors

The LIG fabricated on the LIPM films exhibited good conductive properties relative to the non-conductive LIPM film. This served as an opportunity for the LIG on LIPM film to serve as a layer of conductive circuitry on a flexible and stretchable substrate. To exploit the phenomena, we fabricated a simple pressure sensor using LIG, as a proof of concept to exhibit the functionality of the LIG produced on graphene films.

3.2.1 Fabrication of LIPM-based pressure sensors

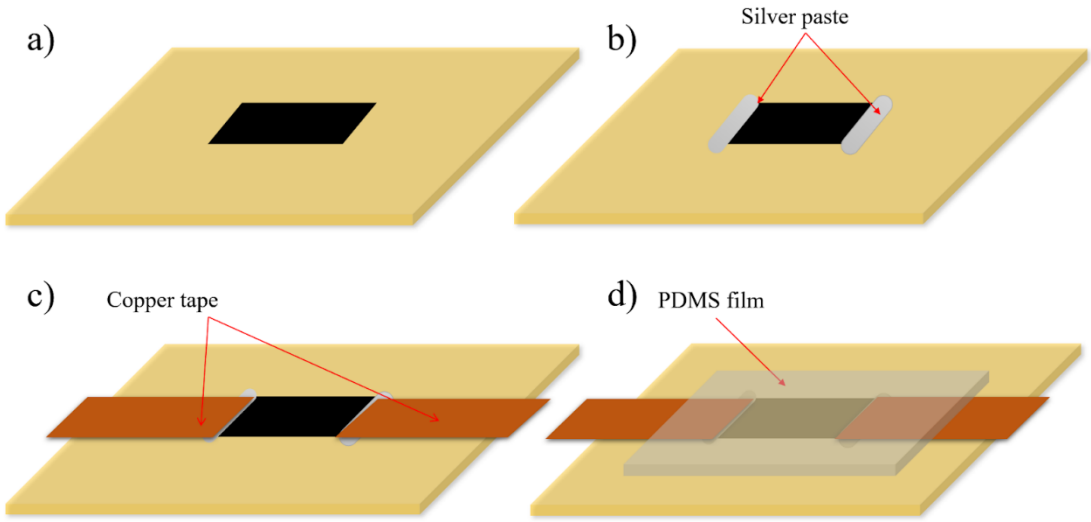

Figure 3.4: Schematic representing the fabrication process of the LIPM pressure sensor.

To employ the LIG as a pressure sensor, we required a larger surface area of LIG onto which a force could be applied, hence we created a patch of LIG by programming the laser accordingly. As can be observed in the schematic shown in Fig. 3.4, the LIG pressure sensor

could be fabricated in 3 simple steps. Note: The LIG25 film and a laser trace speed of 5.6 mm·s^{-1} were chosen to fabricate the sensor in order to showcase LIG performance using median values. Step 1: the laser is used to produce a 1 cm wide patch of LIG. Step 2: Upon completion of the lasing process, an electrical contact was required to measure the electrical response of the LIG. Hence, similar to the resistance measurement setup, Ag paste was applied to both the ends of the LIG patch upon which ~2 cm long pieces of copper tape were fixed followed by curing at room temperature for 24 hrs. This established conductive terminals on either side of the LIG sample. Step 3: To prevent the fragile LIG from crumbling upon the application of force and sticking to the medium applying the force, a thin (~300 μm) layer of PDMS was deposited atop the LIG patch and cured at 80°C for 20 min. The pressure sensor could now be connected to the Keithley sourcemeter and tested for sensing applications.

3.2.2 Characterization of LIPM-based pressure sensors

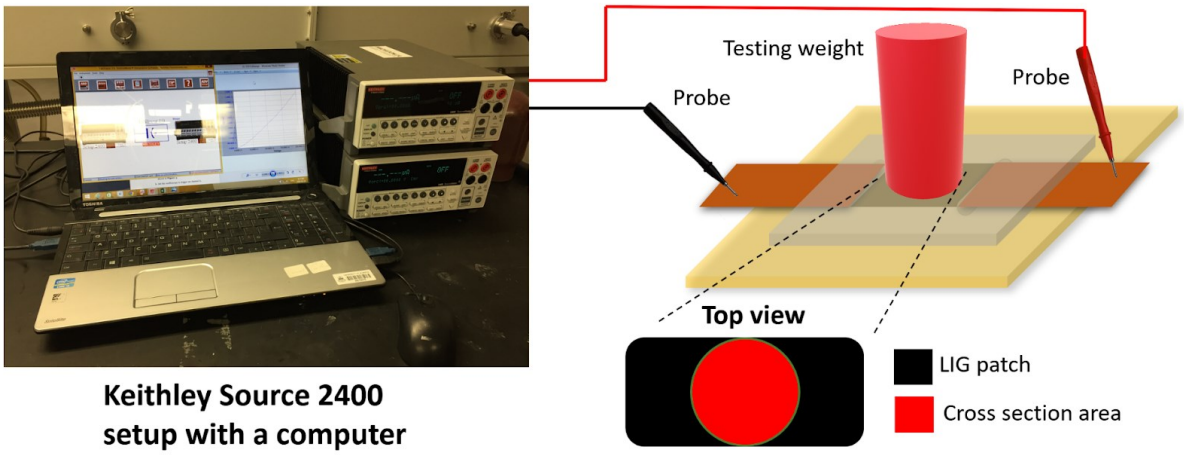

Figure 3.5: The electrical setup used to sense the pressure response. The testing weight was mounted onto the LIPM sensor as shown. The area of cross section in red was the region of contact between the weight and the film.

Five different weights were used to test the pressure sensor response. These different weights spanned a pressure range of 350 Pa – 900 Pa. The pressure weights were made using glass vials for which the weight was modulated via the addition of objects inside the vials. The weights were precisely measured using a weighing scale. The vials were kept on the flat top side to ensure the force was evenly distributed, hence the pressure was applied across the circular region on the 1 cm wide patch. The schematic in Fig. 3.5 shows the experimental setup for measure the pressure sensor response.

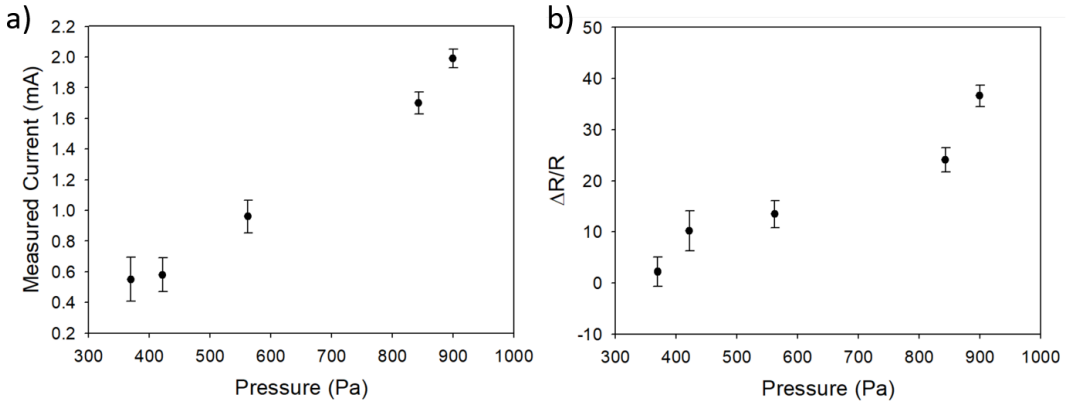

Figure 3.6: (a) Current response upon the addition of respective pressures onto the LIPM sensor. (b) The *ΔR/R* responsivity curve of the LIPM sensor.

A constant electric potential of 10V was applied across the copper tapes and the current response was continuously measured. The different weights were added on top of the sensor and then lifted after a few seconds while the current response was being monitored.

Fig. 3.6a shows the current response observed for 5 different weights i.e. pressure values. Our LIG pressure sensor on LIPM films is a static pressure sensor, it can identify a change in pressure and give a continuous output signal that is proportional to the applied force. It can be inferred from Fig. 3.6a, that upon applying higher pressures, the conductivity of the sensor increases thereby generating larger currents up to a few mA. The *ΔR/R* response shown in Fig. 3.6b, observably increases with applied pressures, indicating higher response for larger

pressures in the testing range while accommodating viable sensitivity in the low-pressure range. This must be explained due to the porous structure of LIG which is able to retain good conductive structures in relaxed and compressed states.

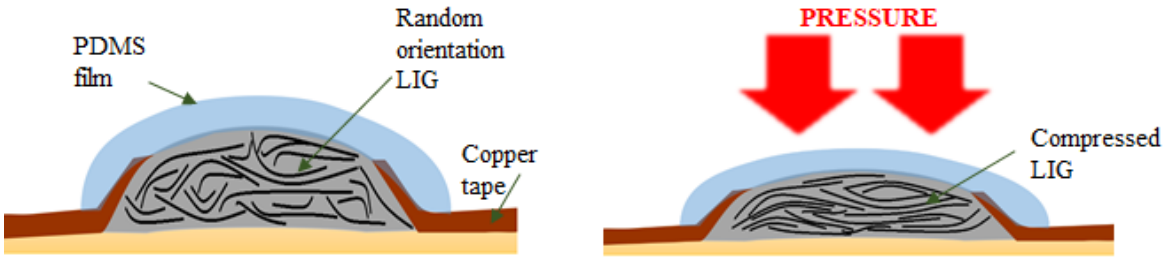

Figure 3.7: Schematic showing the compression mechanism upon the application of a force on the LIPM pressure sensor.

We hypothesize the pressure applied to this sensor causes the deformed porous graphitic structures in random orientations to compress momentarily and form stacks of multiple stacked 2D sheets reducing the deformities as represented in Fig. 3.7a, thereby increasing the 2D cross-linking of multiple LIG pieces to give peak currents as seen in Fig. 3.7b.

This differentiates the LIPM sensor from most electronic pressure sensors that sense the change either via current induction in piezoelectric sensors or current drops caused by deformation leading to change in capacitance. The LIG mechanism differs as it relies on formation of conductive pathways. However, a pressure limit until which the compression causes no irreversible damage to the LIG structures must exist, which is to be explored in a future study. The tested pressure range lies in the sensitive-light touch region which can find utility in light-object interaction detectors or as touch sensors.

Our LIPM sensors also have the potential to be used as strain sensors, though the demonstration is yet to be made. In order to test the strain or of an active material in the strain sensor and assess the parameters within which the functioning of the sensor is limited to, a study to determine the gauge factor should be conducted. Gauge factor is the ratio of the resistive change to the strain of the active material being tested as given by the following equation: GF = $(\Delta R/R)/(\Delta L/L)$, where $\Delta R/R$ is the resistive response and $\Delta L/L$ is the strain of the active material. For our study, we faced the challenges to accurately determine the gauge factor as the amount of strain produced could not calculated due to the highly thin nature of the LIPM film and lack of appropriate experimental tools to measure the strain produced. A future study on gauge factor is important, as it will be able to help us accurately determine the performance characteristics and the robust physical properties of the LIPM film.

3.3 Summary

A working model of LIPM-based pressure sensors has been demonstrated in the work above. The IV characteristics and responsivity show promise in the sensitivity of the device. By using LIG as the sensing element, the LIPM-based pressure sensor is capable of detecting pressures from a few hundred Pa to ~1 kPa as can be observed from the current response of the sensor upon application of a force. An effective method has been demonstrated to showcase the utility of the LIG produced on the LIPM films to serve as electronic circuitry.

There are reports [101, 102] of pressure sensors employing other types of graphene. Our pressure sensors with LIG are compared with these reported devices and analysed in the table shown below.

	This work	**Graphene based piezo-resistive pressure sensor [101]**	**Pressure sensors based on graphene hybrids [102]**
Film structure	LIG structure covered with PDMS film.	SiN sheets with a bridge for maximum strain, onto CVD graphene.	AuNPs coated cystamines sandwiched between graphene layers.
Working mechanism	Pressing the sensor leads to formation of conductive pathways in LIG, i.e. parallel conductive layers of graphene.	Piezo-resistive pressure sensor. Deflection of the membrane causes a change in strain leading to change in graphene resistance.	Improvement in resistance change upon pressure due to enhanced charge transfer in graphene functionalized AuNPs.
Overall (Performance + Cost-effectiveness + fabrication)	Touch sensitive sensor. (300- 900Pa, higher pressures not tested) Low cost. Simple fabrication. Biocompatible + Bio-degradable.	Large range of sensitivity (1Pa – 70kPa). Expensive. Fabrication requires ion-beam etching and CVD.	Sensitive pressure sensor (86Pa - 56kPa). Expensive. Complex fabrication procedure: vacuum filtrations to prepare AuNPs then preparing graphene sandwiched structure.

Chapter 4

Conclusions and future works

4.1 Conclusions

Production rates of graphene have consistently risen this past decade where several techniques have been refined to optimize the production quality and quantity of graphene. The laser induction process, to produce graphene from commercial PI films was the first used in 2014. Due to its cost effectiveness and low consumption of readily available resources, it can possibly serve as the dominant technique employed to produce graphene for several applications. Since 2014, several studies on techniques and substrates to produce LIG have been explored and refined, but there is a lack of research done on substrates that are inexpensive, renewable (environment friendly) and stretchable/ flexible at the same time.

My choice of lignin, discussed in Chapter 2, which is an abundantly available inexpensive renewable resource, has been demonstrated in the work above to serve as a viable substrate for producing LIG as confirmed by Raman spectroscopy. Fairly simple methods are employed to fabricate the LIPM films without the use of any complex tools which makes the LIPM substrate attractive for an industry which prefers low production costs. Laser induction onto these films can be automated to produce a variety of electrical circuitry, which added atop the extant features like biocompatibility and durability of the LIPM films brought about by lignin and PDMS, enables a wide variety of applications such as sensors, filters and supercapacitors for electronics, chemical and the biomedical industry. A further drop in expense can be incurred during industrial manufacturing if mass production processes such as a roll to roll fabrication process is employed.

Inferring from the pressure sensor that has been shown as a proof of concept in Chapter 3, LIG on LIPM films can be considered a suitable candidate for making electronic circuitry on flexible/-stretchable LIPM substrates. The LIPM films are inexpensive to fabricate and are made from a renewable resource. Light-touch based electronics applications lie in the range exhibited by the pressure sensor. The change in pressure is recorded via an increase in the current flowing through the sensor which can be used to drive a small LED indicating pressure detection or drive another small circuit coupled through an amplifier.

4.2 Future works

Further characterization of the chemical composition of the lased LIPM substrate is required in future studies, and it will enable better understanding of LIG quality. These characterization techniques should include UV/Vis absorption, X-Ray photoelectron spectroscopy (XPS) and energy dispersive X-ray spectroscopy (EDS). The UV-Vis absorption spectroscopy will help us identify any oxidized by-products from the lasing process, since these oxidized by-products are organic molecules and may absorb light in the near visible and visible regions. XPS will unveil the percentage of lignin converted to graphene by identifying and measuring the amount of various carbon states. This study on LIG with various lasing conditions and lignin concentration will help to determine how the high-quality graphene without any oxidized products can be produced. EDS can be used to do a depth analysis of chemical elements in the lased LIPM film to ascertain the depth of penetration of the laser beam and MLG formation to understand any relation between depth and LIG quality. More accurate resistance measurements of produced LIG should be made using the 4 point-probe measurement. Furthermore, a wheatstone bridge can also be integrated to the circuit to make it sensitive and reduce error in any measurements.

Apart from the characterization, there are two facets for development of LIG on LIPM films. One, the technique used to fabricate the LIG on LIPM film to improve the quality of the LIG itself and second, developing the sensor to diversify its applications.

4.2.1 LIPM fabrication methods

LIG production for our studies was done in an ambient atmosphere to elicit the cost-effectiveness of the production method and resources required. But as we know from section 1.2, removal of oxygen is prioritized in most graphene production processes as it hampers the conductivity of the whole sample. Hence, fabrication in a vacuum or N_2 environment, which has not been explored in this study could possibly lead to higher quality LIG with even lower resistivity. Previous studies done controlled atmospheres have been used for obtaining diverse functionalities out of LIG [103], where superhydrophobic and superhydrophilic surfaces have been prepared due to a large change in the contact angle with the water.

A study on repetitive lasing on the same spot, such as the multiple lasing using defocus method [43] could be explored, which might be promising for the consequent LIG quality as the defocus study was done directly onto wooden and paper substrates. Also, this study employed unidirectional and parallel line lasing to produce test samples and the patches for the pressure sensor. A study that stems from the multiple lasing method, is one where we study the effect on LIG quality produced if multiple laser traces intersect and overlap at different angles, which could possibly provide data that is in contrast with the extant techniques deployed for obtaining LIG.

4.2.2 Extending functionality via applications

There are a range of applications that could be explored with higher quality LIG. Further studies characterizing the LIG on LIPM films can extend its applicability as different properties could be enhanced.

As discussed in the previous section (section 4.2.1), future studies on the elastic moduli of the LIPM film can really define the limits to the stretchability of the LIPM films. Modulating the curing agent and polymer ratio in PDMS and studying the adhesion of the resulting LIG on these films can be used to ascertain whether the LIG will retain its physical structure without breaking or will it retain its adhesion to the LIPM substrate under the excessive stress. Several studies have also doped LIG with other elements such as Boron (B) to achieve microsupercapacitors [45] or Sulphur (S) to produce antimicrobial surfaces [46]. Doping could possibly be tried to further widen the areas of applicability of this sensor. Another study on the electrical properties of superimposed LIGs for a pressure sensor application, where the LIG atop the the LIPM film is flipped to precisely overlap the LIG underneath with LIG on another LIPM film could also reveal interesting results. MLG exhibits various exotic electronic properties compared to SLG which does not have a bandgap. Further studying LIG on LIPM substrates can be explored for optoelectronic applications such as photodetectors in [103].

References

[1] Geim, A. K., and Novoselov, K. S. “The rise of graphene,” Nature Materials, V. 6, No. 3, 2007, pp. 183–91.

[2] Cooper, D. R., D’Anjou, B., Ghattamaneni, N., et al. “Experimental Review of Graphene,” ISRN Condensed Matter Physics, V. 2012, 2012, pp. 1–56.

[3] Fathi, D. “A Review of Electronic Band Structure of Graphene and Carbon Nanotubes Using Tight Binding,” Journal of Nanotechnology, V. 2011, 2011, pp. 1–6.

[4] Dato, A., Lee, Z., Jeon, K.-J., et al. “Clean and highly ordered graphene synthesized in the gas phase,” Chemical Communications, No. 40, 2009, p. 6095.

[5] Bolotin, K. I., Ghahari, F., Shulman, M. D., et al. “Observation of the fractional quantum Hall effect in graphene,” Nature, V. 462, No. 7270, 2009, pp. 196–9.

[6] Novoselov, K. S., Geim, A. K., Morozov, S. V., et al. “Two-dimensional gas of massless Dirac fermions in graphene,” Nature, V. 438, No. 7065, 2005, pp. 197–200.

[7] Morozov, S. V., Novoselov, K. S., Katsnelson, M. I., et al. “Giant Intrinsic Carrier Mobilities in Graphene and Its Bilayer,” Physical Review Letters, V. 100, No. 1, 2008.

[8] Castro Neto, A. H., Guinea, F., Peres, N. M. R., et al. “The electronic properties of graphene,” Reviews of Modern Physics, V. 81, No. 1, 2009, pp. 109–62.

[9] Chen, J.-H., Jang, C., Xiao, S., et al. “Intrinsic and extrinsic performance limits of graphene devices on SiO2,” Nature Nanotechnology, V. 3, No. 4, 2008, pp. 206–9.

[10] Cai, W., Moore, A. L., Zhu, Y., et al. “Thermal Transport in Suspended and Supported Monolayer Graphene Grown by Chemical Vapor Deposition,” Nano Letters, V. 10, No. 5, 2010, pp. 1645–51.

[11] Field, J. E.,”The Properties of diamond”, London New York: Academic Press, 1979.

[12] Heyrovska R., “Atomic Structures of Graphene, Benzene and Methane with Bond Lengths as Sums of the Single, Double and Resonance Bond Radii of Carbon”. arXiv, General Physics, arXiv:0804.4086.

[13] Lee, C., Wei, X., Kysar, J. W., et al. “Measurement of the Elastic Properties and Intrinsic Strength of Monolayer Graphene,” Science, V. 321, No. 5887, 2008, pp. 385–8.

[14] Zhang, Y., Tang, T.-T., Girit, C., et al. “Direct observation of a widely tunable bandgap in bilayer graphene,” Nature, V. 459, No. 7248, 2009, pp. 820–3.

[15] Lungerich, D., Papaianina, O., Feofanov, M., et al. “Dehydrative π-extension to nanographenes with zig-zag edges,” Nature Communications, V. 9, No. 1, 2018.

[16] Denis, P. A., and Iribarne, F. “Comparative Study of Defect Reactivity in Graphene,” The Journal of Physical Chemistry C, V. 117, No. 37, 2013, pp. 19048–55.

[17] Wang, K., Ruan, J., Song, H., et al. “Biocompatibility of Graphene Oxide,” Nanoscale Research Letters, 2010.

[18] https://www.grandviewresearch.com/industry-analysis/graphene-industry

[19] Wang, X.-Y., Narita, A., and Müllen, K. “Precision synthesis versus bulk-scale fabrication of graphenes,” Nature Reviews Chemistry, V. 2, No. 1, 2017.

[20] Jayasena, B., and Subbiah, S. “A novel mechanical cleavage method for synthesizing few-layer graphenes,” Nanoscale Research Letters, V. 6, No. 1, 2011.

[21] Hofmann, M., Chiang, W.-Y., D Nguyễn, T., et al. “Controlling the properties of graphene produced by electrochemical exfoliation,” Nanotechnology, V. 26, No. 33, 2015, p. 335607.
[22] Park, S., and Ruoff, R. S. “Chemical methods for the production of graphenes,” Nature Nanotechnology, V. 4, No. 4, 2009, pp. 217–24.
[23] Griggs C.S., Medina V., “Graphene and graphene oxide membranes for water treatment,” AccessScience, 2016.
[24] Novoselov, K. S., Fal′ko, V. I., Colombo, L., et al. “A roadmap for graphene,” Nature, V. 490, No. 7419, 2012, pp. 192–200.
[25] Eigler, S., Enzelberger-Heim, M., Grimm, S., et al. “Wet Chemical Synthesis of Graphene,” Advanced Materials, V. 25, No. 26, 2013, pp. 3583–7.
[26] Jimenez-Cervantes, E., López-Barroso, J., Martínez-Hernández, A. L., et al. “Graphene-Based Materials Functionalization with Natural Polymeric Biomolecules.” Recent Advances in Graphene Research. InTech, 2016.
[27] León, V., Quintana, M., Herrero, M. A., et al. “Few-layer graphenes from ball-milling of graphite with melamine,” Chemical Communications, V. 47, No. 39, 2011, p. 10936.
[28] Hernandez, Y., Nicolosi, V., Lotya, M., et al. “High-yield production of graphene by liquid-phase exfoliation of graphite,” Nature Nanotechnology, V. 3, No. 9, 2008, pp. 563–8.
[29] Paton, K. R., Varrla, E., Backes, C., et al. “Scalable production of large quantities of defect-free few-layer graphene by shear exfoliation in liquids,” Nature Materials, V. 13, No. 6, 2014, pp. 624–30.
[30] Yang, S., Brüller, S., Wu, Z.-S., et al. “Organic Radical-Assisted Electrochemical Exfoliation for the Scalable Production of High-Quality Graphene,” Journal of the American Chemical Society, V. 137, No. 43, 2015, pp. 13927–32.
[31] Matsumoto, M., Saito, Y., Park, C., et al. “Ultrahigh-throughput exfoliation of graphite into pristine ‘single-layer’ graphene using microwaves and molecularly engineered ionic liquids,” Nature Chemistry, V. 7, No. 9, 2015, pp. 730–6.
[32] Lee, J.-H., Lee, E. K., Joo, W.-J., et al. “Wafer-Scale Growth of Single-Crystal Monolayer Graphene on Reusable Hydrogen-Terminated Germanium,” Science, V. 344, No. 6181, 2014, pp. 286–9.
[33] Bansal, T., Durcan, C. A., Jain, N., et al. “Synthesis of few-to-monolayer graphene on rutile titanium dioxide,” Carbon, V. 55, 2013, pp. 168–75.
[34] de Heer, W. A., Berger, C., Ruan, M., et al. “Large area and structured epitaxial graphene produced by confinement controlled sublimation of silicon carbide,” Proceedings of the National Academy of Sciences, V. 108, No. 41, 2011, pp. 16900–5.
[35] Li, X., Colombo, L., and Ruoff, R. S. “Synthesis of Graphene Films on Copper Foils by Chemical Vapor Deposition,” Advanced Materials, V. 28, No. 29, 2016, pp. 6247–52.
[36] Li, X., Cai, W., An, J., et al. “Large-Area Synthesis of High-Quality and Uniform Graphene Films on Copper Foils,” Science, V. 324, No. 5932, 2009, pp. 1312–4.
[37] Kobayashi, T., Bando, M., Kimura, N., et al. “Production of a 100-m-long high-quality graphene transparent conductive film by roll-to-roll chemical vapor deposition and transfer process,” Applied Physics Letters, V. 102, No. 2, 2013, p. 23112.
[38] Tao, L., Lee, J., Holt, M., et al. “Uniform Wafer-Scale Chemical Vapor Deposition of Graphene on Evaporated Cu (111) Film with Quality Comparable to Exfoliated Monolayer,” The Journal of Physical Chemistry C, V. 116, No. 45, 2012, pp. 24068–74.

[39] Bointon, T. H., Barnes, M. D., Russo, S., et al. “High Quality Monolayer Graphene Synthesized by Resistive Heating Cold Wall Chemical Vapor Deposition,” Advanced Materials, V. 27, No. 28, 2015, pp. 4200–6.
[40] Hao, Y., Bharathi, M. S., Wang, L., et al. “The Role of Surface Oxygen in the Growth of Large Single-Crystal Graphene on Copper,” Science, V. 342, No. 6159, 2013, pp. 720–3.
[41] Carvalho, A. F., Fernandes, A. J. S., Leitão, C., et al. “Laser-Induced Graphene Strain Sensors Produced by Ultraviolet Irradiation of Polyimide,” Advanced Functional Materials, V. 28, No. 52, 2018, p. 1805271.
[42] Lin, J., Peng, Z., Liu, Y., et al. “Laser-induced porous graphene films from commercial polymers,” Nature Communications, V. 5, No. 1, 2014.
[43] Chyan, Y., Ye, R., Li, Y., et al. “Laser-Induced Graphene by Multiple Lasing: Toward Electronics on Cloth, Paper, and Food,” ACS Nano, V. 12, No. 3, 2018, pp. 2176–83.
[44] Ye, R., Peng, Z., Wang, T., et al. “In Situ Formation of Metal Oxide Nanocrystals Embedded in Laser-Induced Graphene,” ACS Nano, V. 9, No. 9, 2015, pp. 9244–51.
[45] Peng, Z., Ye, R., Mann, J. A., et al. “Flexible Boron-Doped Laser-Induced Graphene Microsupercapacitors,” ACS Nano, V. 9, No. 6, 2015, pp. 5868–75.
[46] Singh, S. P., Li, Y., Zhang, J., et al. “Sulfur-Doped Laser-Induced Porous Graphene Derived from Polysulfone-Class Polymers and Membranes,” ACS Nano, V. 12, No. 1, 2017, pp. 289–97.
[47] Lamberti, A., Serrapede, M., Ferraro, G., et al. “All-SPEEK flexible supercapacitor exploiting laser-induced graphenization,” 2D Materials, V. 4, No. 3, 2017, p. 35012.
[48] Zhang, Z., Song, M., Hao, J., et al. “Visible light laser-induced graphene from phenolic resin: A new approach for directly writing graphene-based electrochemical devices on various substrates,” Carbon, V. 127, 2018, pp. 287–96.
[49] Ye, R., Chyan, Y., Zhang, J., et al. “Laser-Induced Graphene Formation on Wood,” Advanced Materials, V. 29, No. 37, 2017, p. 1702211.
[50] Ye, R., James, D. K., and Tour, J. M. “Laser-Induced Graphene: From Discovery to Translation,” Advanced Materials, V. 31, No. 1, 2018, p. 1803621.
[51] Duy, L. X., Peng, Z., Li, Y., et al. “Laser-induced graphene fibers,” Carbon, V. 126, 2018, pp. 472–9.
[52] You, R., Liu, Y., Hao, Y., et al. “Laser Fabrication of Graphene-Based Flexible Electronics,” Advanced Materials, 2019, p. 1901981.
[53] Clerici, F., Fontana, M., Bianco, S., et al. “In situ MoS2 Decoration of Laser-Induced Graphene as Flexible Supercapacitor Electrodes,” ACS Applied Materials & Interfaces, V. 8, No. 16, 2016, pp. 10459–65.
[54] Stanford, M. G., Yang, K., Chyan, Y., et al. “Laser-Induced Graphene for Flexible and Embeddable Gas Sensors,” ACS Nano, V. 13, No. 3, 2019, pp. 3474–82.
[55] Li, C., Zhang, X., Wang, K., et al. “Scalable Self-Propagating High-Temperature Synthesis of Graphene for Supercapacitors with Superior Power Density and Cyclic Stability,” Advanced Materials, V. 29, No. 7, 2016, p. 1604690.
[56] Zheng, Y., Bai, H., Huang, Z., et al. “Directional water collection on wetted spider silk,” Nature, V. 463, No. 7281, 2010, pp. 640–3.

[57] Ataka, K., Stripp, S. T., and Heberle, J. “Surface-enhanced infrared absorption spectroscopy (SEIRAS) to probe monolayers of membrane proteins,” Biochimica et Biophysica Acta (BBA) - Biomembranes, V. 1828, No. 10, 2013, pp. 2283–93.

[58] Mamleyev, E. R., Heissler, S., Nefedov, A., et al. “Laser-induced hierarchical carbon patterns on polyimide substrates for flexible urea sensors,” npj Flexible Electronics, V. 3, No. 1, 2019.

[59] Tan, K. W., Jung, B., Werner, J. G., et al. “Transient laser heating induced hierarchical porous structures from block copolymer–directed self-assembly,” Science, V. 349, No. 6243, 2015, pp. 54–8.

[60] Zhang, C., Lv, W., Tao, Y., et al. “Towards superior volumetric performance: design and preparation of novel carbon materials for energy storage,” Energy & Environmental Science, V. 8, No. 5, 2015, pp. 1390–403.

[61] Kyerematen, N. A., Brousse, T., and Pech, D. “Microsupercapacitors as miniaturized energy-storage components for on-chip electronics,” Nature Nanotechnology, V. 12, No. 1, 2016, pp. 7–15.

[62] Beidaghi, M., and Gogotsi, Y. “Capacitive energy storage in micro-scale devices: recent advances in design and fabrication of micro-supercapacitors,” Energy & Environmental Science, V. 7, No. 3, 2014, p. 867.

[63] Chmiola, J., Largeot, C., Taberna, P. L., et al. “Monolithic Carbide-Derived Carbon Films for Micro-Supercapacitors,” Science, V. 328, No. 5977, 2010, pp. 480–3.

[64] El-Kady, M. F., and Kaner, R. B. “Scalable fabrication of high-power graphene micro-supercapacitors for flexible and on-chip energy storage,” Nature Communications, V. 4, No. 1, 2013.

[65] Gao, W., Singh, N., Song, L., et al. “Direct laser writing of micro-supercapacitors on hydrated graphite oxide films,” Nature Nanotechnology, V. 6, No. 8, 2011, pp. 496–500.

[66] Pech, D., Brunet, M., Durou, H., et al. “Ultrahigh-power micrometre-sized supercapacitors based on onion-like carbon,” Nature Nanotechnology, V. 5, No. 9, 2010, pp. 651–4.

[67] Peng, Z., Lin, J., Ye, R., et al. “Flexible and Stackable Laser-Induced Graphene Supercapacitors,” ACS Applied Materials & Interfaces, V. 7, No. 5, 2015, pp. 3414–9.

[68] Yang, P., Zhao, D., Margolese, D. I., et al. “Generalized syntheses of large-pore mesoporous metal oxides with semicrystalline frameworks,” Nature, V. 396, No. 6707, 1998, pp. 152–5.

[69] Joo, S. H., Choi, S. J., Oh, I., et al. “Ordered nanoporous arrays of carbon supporting high dispersions of platinum nanoparticles,” Nature, V. 412, No. 6843, 2001, pp. 169–72.

[70] Peinemann, K.-V., Abetz, V., and Simon, P. F. W. “Asymmetric superstructure formed in a block copolymer via phase separation,” Nature Materials, V. 6, No. 12, 2007, pp. 992–6.

[71] Gan, Z., Cao, Y., Evans, R. A., et al. “Three-dimensional deep sub-diffraction optical beam lithography with 9 nm feature size,” Nature Communications, V. 4, No. 1, 2013.

[72] Kawata, S., Sun, H.-B., Tanaka, T., et al. “Finer features for functional microdevices,” Nature, V. 412, No. 6848, 2001, pp. 697–8.

[73] Ye, R., del Angel-Vicente, P., Liu, Y., et al. “High-Performance Hydrogen Evolution from MoS2(1-x)PxSolid Solution,” Advanced Materials, V. 28, No. 7, 2015, pp. 1427–32.

[74] Tehrani, F., Beltrán-Gastélum, M., Sheth, K., et al. “Laser-Induced Graphene Composites for Printed, Stretchable, and Wearable Electronics,” Advanced Materials Technologies, V. 4, No. 8, 2019, p. 1900162.
[75] An, J., Le, T.-S. D., Huang, Y., et al. “All-Graphene-Based Highly Flexible Noncontact Electronic Skin,” ACS Applied Materials & Interfaces, V. 9, No. 51, 2017, pp. 44593–601.
[76] Wang, D.-Y., Tao, L.-Q., Liu, Y., et al. “High performance flexible strain sensor based on self-locked overlapping graphene sheets,” Nanoscale, V. 8, No. 48, 2016, pp. 20090–5.
[77] Qiao, Y., Wang, Y., Tian, H., et al. “Multilayer Graphene Epidermal Electronic Skin,” ACS Nano, V. 12, No. 9, 2018, pp. 8839–46.
[78] Sun, B., McCay, R. N., Goswami, S., et al. “Gas-Permeable, Multifunctional On-Skin Electronics Based on Laser-Induced Porous Graphene and Sugar-Templated Elastomer Sponges,” Advanced Materials, V. 30, No. 50, 2018, p. 1804327.
[79] An, J., Le, T.-S. D., Lim, C. H. J., et al. “Single-Step Selective Laser Writing of Flexible Photodetectors for Wearable Optoelectronics,” Advanced Science, V. 5, No. 8, 2018, p. 1800496.
[80] Nishimura, H., Kamiya, A., Nagata, T., et al. “Direct evidence for α ether linkage between lignin and carbohydrates in wood cell walls,” Scientific Reports, V. 8, No. 1, 2018.
[81] https://en.wikipedia.org/wiki/Lignin
[82] Zhu, H., Luo, W., Ciesielski, P. N., et al. “Wood-Derived Materials for Green Electronics, Biological Devices, and Energy Applications,” Chemical Reviews, V. 116, No. 16, 2016, pp. 9305–74.
[83] Adler, E. “Lignin chemistry?past, present and future,” Wood Science and Technology, V. 11, No. 3, 1977, pp. 169–218.
[84] Kawamoto, H. “Lignin pyrolysis reactions,” Journal of Wood Science, V. 63, No. 2, 2017, pp. 117–32.
[85] Li, X., and Chapple, C. “Understanding Lignification: Challenges Beyond Monolignol Biosynthesis: Figure 1.,” Plant Physiology, V. 154, No. 2, 2010, pp. 449–52.
[86] Wang, Y., Chantreau, M., Sibout, R., et al. “Plant cell wall lignification and monolignol metabolism,” Frontiers in Plant Science, V. 4, 2013.
[87] Chen, Y., and Sarkanen, S. “Macromolecular replication during lignin biosynthesis,” Phytochemistry, V. 71, No. 4, 2010, pp. 453–62.
[88] Luo Y.R.,”Comprehensive handbook of chemical bond energies”, Boca Raton: CRC Press, 2007, pp. 161.
[89] Schutyser, W., Renders, T., Van den Bosch, S., et al. “Chemicals from lignin: an interplay of lignocellulose fractionation, depolymerisation, and upgrading,” Chemical Society Reviews, V. 47, No. 3, 2018, pp. 852–908.
[90] Brannon, J. H., Lankard, J. R., Baise, A. I., et al. “Excimer laser etching of polyimide,” Journal of Applied Physics, V. 58, No. 5, 1985, pp. 2036–43.
[91] FALKEHAG, S. I., MARTON, J., and ADLER, E. “Chromophores in Kraft Lignin.” Advances in Chemistry. AMERICAN CHEMICAL SOCIETY, 1966. pp. 75–89.
[92] Patwardhan, P. R., Brown, R. C., and Shanks, B. H. “Product Distribution from the Fast Pyrolysis of Hemicellulose,” ChemSusChem, V. 4, No. 5, 2011, pp. 636–43.

[93] Dovbeshko, G., Fesenko, O., Dementjev, A., et al. “Coherent anti-Stokes Raman scattering enhancement of thymine adsorbed on graphene oxide,” Nanoscale Research Letters, V. 9, No. 1, 2014.
[94] Wu, J.-B., Lin, M.-L., Cong, X., et al. “Raman spectroscopy of graphene-based materials and its applications in related devices,” Chemical Society Reviews, V. 47, No. 5, 2018, pp. 1822–73.
[95] Ferrari, A. C., Meyer, J. C., Scardaci, V., et al. “Raman Spectrum of Graphene and Graphene Layers,” Physical Review Letters, V. 97, No. 18, 2006.
[96] Cai, D., Neyer, A., Kuckuk, R., et al. “Raman, mid-infrared, near-infrared and ultraviolet–visible spectroscopy of PDMS silicone rubber for characterization of polymer optical waveguide materials,” Journal of Molecular Structure, V. 976, Nos. 1–3, 2010, pp. 274–81.
[97] https://en.wikipedia.org/wiki/Pressure_measurement
[98] https://instrumentationtools.com/c-bourdon-tube-theory/
[99] https://instrumentationtools.com/capacitive-pressure-sensor/
[100] https://www.st.com/resource/en/datasheet/lps22hh.pdf
[101] Zhu, S.-E., Krishna Ghatkesar, M., Zhang, C., et al. “Graphene based piezoresistive pressure sensor,” Applied Physics Letters, V. 102, No. 16, 2013, p. 161904.
[102] Vaka, M., Bian, M. Z., and Nam, N. D. “Highly sensitive pressure sensor based on graphene hybrids,” Arabian Journal of Chemistry, V. 13, No. 1, 2020, pp. 1917–23.
[103] Li, Y., Luong, D. X., Zhang, J., et al. “Laser-Induced Graphene in Controlled Atmospheres: From Superhydrophilic to Superhydrophobic Surfaces,” Advanced Materials, V. 29, No. 27, 2017, p. 1700496.
[104] Karamat, S., Sonuşen, S., Çelik, Ü., et al. “Synthesis of few layer single crystal graphene grains on platinum by chemical vapour deposition,” Progress in Natural Science: Materials International, V. 25, No. 4, 2015, pp. 291–9.